Title
Design, Fabrication and Characterization of a Plasmonic Haloscope Resonator for the Detection of Axionic Dark Matter

Author
Al Kenany, Saad

Publication Date
2021

Peer reviewed|Thesis/dissertation

Design, Fabrication, and Characterization of a Plasmonic Haloscope Resonator for the Detection of Axionic Dark Matter

By

Saad Al Kenany

A dissertation submitted in partial satisfaction of the
requirements for the degree of

Doctor of Philosophy

in

Engineering- Nuclear Engineering

in the

Graduate Division

of the

University of California, Berkeley

Committee in Charge:

Professor Karl van Bibber, Chair
Professor David Attwood
Professor Ka-Ngo Leung

Spring 2021

Design, Fabrication and Characterization of a Plasmonic Haloscope Resonator for Detection of Axionic Dark Matter

by

Saad Al Kenany

Abstract

Design, Fabrication and Characterization of a Plasmonic Haloscope Resonator for the Detection of Axionic Dark Matter

By

Saad Al Kenany

Department of Nuclear Engineering, University of California Berkeley

Professor Karl van Bibber, Chair

From astronomical observations and theories of standard cosmological models, we infer the existence of a large unobserved component of mass in the universe that is not luminous but evident through its gravitational interactions with ordinary matter. We call this unobserved component "dark matter". Various theoretical solutions to the nature of dark matter come from beyond-Standard Model theories. One possible solution to its composition is a particle called the axion. As with all candidates, direct detection of the dark matter particle will be required to confirm the theoretical hypothesis. For the axion, the principle experiments in this mass range with sensitivity to the standard axion are ADMX (formerly at LLNL, now the University of Washington), CAPP (Korea) and HAYSTAC (at Yale). These experiments, operating in the GHz range, are based on the principle that the axion may resonantly convert to a single photon in a microwave cavity permeated by a magnetic field. This modality is convenient for the (0.1-10) GHz range, roughly corresponding to the (0.4-40) μeV mass range, but the axion might be much higher in mass. There is a practical limitation to searching for the axion by this technique at much higher masses, owing to the fact that much higher frequency resonators are intrinsically much smaller, and thus the conversion power would become undetectably small.

A solution to achieving a usably large volume (and thus higher signal power) with a resonator of a desired high frequency (e.g., 10-100 GHz) was proposed by the Wilczek theory group at Stockholm University in 2019. This technique involves a 3D array of very thin wires, a metamaterial that mimics a plasma, the plasma frequency of which can be designed to correspond to very high frequencies. Our Berkeley group has entered a collaboration with the Stockholm group to provide experimental support to validate the

fundamental theory of plasmonic resonators, to explore the most practical ways by which such a metamaterial may be tuned in frequency, and ultimately to provide a pre-conceptual design for a full-scale experiment.

This thesis primarily focused on the first two goals. Towards the first goal, a series of wire frames were produced and strung with gold-coated tungsten wires of 50μm diameter, spaced by 5.38 mm, and stacked together. The microwave transmission through this stack (i.e., S_{21}) was measured as a function of frequency to determine the plasma frequency ω_p, for various configurations of the wire planes, and compared with the theories of wire-array metamaterials; the agreement was very good. Changing the interplane spacing was found to be the most effective way of tuning the array, and a large dynamic range, nearly a factor of 2, could be achieved by doubling the plane spacing. For the second goal, alternative configurations of wire planes were explored for which there is no currently worked-out theory (rotation of alternate planes relative to the microwave polarization axis; changing the unit cell of the wire array from rectangular to parallelogram but without changing the average density); these produced no useful effect. However, a practical design was conceived by which the spacing of a large number of planes could be accurately and smoothly accomplished, although a prototype was not attainable due to the restricted work conditions of the pandemic. A larger-scale engineering implementation was envisioned, but further work, both theoretical and experimental, remains in how to improve the quality factor of the array, as well as how it could be feasibly read out before such a design could be realized.

To my wife

Table of Contents

List of Tables

List of Figures

Acknowledgments

I am grateful to all the people who supported me during my time in graduate school. My thanks go first to my advisor and mentor, Professor Karl van Bibber, who made this work possible with his unlimited support, guidance, and encouragement. Thank you, Karl!

My thanks extend to my committee members, Professor David Attwood and Professor Ka-Ngo Leung, from LBNL. Thank you, Professor Attwood, for allowing me to attend the AST210 Class Fall 2019, one of my favorite classes ever. I acknowledge Professor Bernard Sadoulet, who gave me the opportunity to work on CDMS, my first dark matter research project. Thank you, Bernard!

In our acknowledgements, my thanks go to Professor Frank Wilczek (MIT) for reaching out to us with a proposal for collaboration, and the contributions of his team, especially Alex Millar and Matthew Lawson from Stockholm University.

No work could progress without teamwork. My special thanks to Alex Droster, who supported me with all the experiments in Lab1140 and showed excellent teamwork, discipline, and professionalism. My thanks go to my colleague Dajie Sun for his support in preparing me for the Neutronics and Radioactive Waste management exams. I also acknowledge Dajie's involvement in the least-squares fitting programs in Mathematica.

Thank you, Professor Lee Bernstein, for your patience and for tutoring me in Nuclear Physics NE101. My thanks to Professor Peter Hosemann, who made his lectures in Material Science NE120 a delightful experience. My thanks to our academic advisor, Professor Kai Vetter, who always had the time to listen to my concerns and enriched me with the best advice.

Thanks to the HAYSTAC collaboration for their support and teamwork spirit. Thank you, Maria Simanovskaia, for your consultation and advice during the past four years of graduate school. My best thanks to Kirsten Wimple Hall! You've always been a helper with heart and a supporter with knowledge.

My special thanks go to my family, especially my patient wife Ursula Kugel-Kenany, my son Jafar Felix Michael, and my daughter Zainab Julia Anna. Thank you for your patience and endless support. They saw the struggle and the ups and downs of graduate school but never stopped encouraging me to proceed.

My thanks to my youngest brother Ziad Carlos, who lives in Sweden, for listening to my concerns and for sharing his sympathy and comfort.

I acknowledge the support of the National Science Foundation under grant number 191419.

Chapter 1

Introduction & Overview

In this chapter, I lay out the limiting factors of microwave cavities in axion search and the various modes of TM, TE, and TME of electromagnetic waves. I present 3D wire arrays as a concept for the detection of axions at higher frequencies (7 to 12 GHz).

1.1 Introduction & Overview

One of the primary limitations of the microwave cavity experiment searching for axions is extending the reach of the experiment to higher masses. As will be seen, this limitation owes to the resonant conversion condition that the frequency of the cavity must equal the mass of the axion, or put quantitatively, $h\nu = m_a c^2$. For the mode which couples most effectively to the axion, i.e., the TM_{010} mode, the radius of the cavity goes inversely to the frequency of the cavity [1]. To avoid mode interference from a proliferation of modes that do not couple to the axion, the TE, and TEM modes, the cavity should not be too long, driving one to maintain a roughly identical aspect ratio. This implies a highly unfavorable scaling whereby the conversion power, which is proportional to the volume of the cavity, goes as f^{-3}. Three concepts have been explored to achieving higher frequencies while maximizing the usable volume in the magnet, such as utilizing a higher order mode TM_{0n0}, loading the cavity with a regular lattice array of metal rods, or phase combining multiple small cavities. While all partially solve the problem, none represents a clear winner; each has other drawbacks which render it less than completely practical.

In this work, I explore a new concept for the detection of axionic mass at higher frequencies, which is to construct a metamaterial consisting of a 3D array of very thin wires. This effectively behaves as a zero-temperature plasma, where the axion couples to a plasmonic excitation of the metamaterial at its plasma frequency. The plasma frequency, in turn, is determined by the radius and spacing of the wires but not the overall dimensions of the array. In this case, the operative frequency is thus uncoupled from the volume of the array, and the array can be built arbitrarily large. In this thesis, I present the work from concept to design, fabrication, testing and characterization of the

detector. The specific proposal to design an axion experiment based on a metamaterial pseudo-plasma, the so-called tunable plasmonic haloscope, is due to Lawson et al. [2] of the Stockholm theory group of Frank Wilczek, who reached out to us in 2018 to suggest a collaboration by which our Berkeley group would provide experimental support and validation for their theory, and ultimately develop a fully engineered array for a large-scale experiment.

In Ch.1, I lay out the structure of my thesis. I start by introducing the problem of the inferred but unobserved mass in the universe referred to as the dark matter in Ch. 2. I discuss various existing experiments for the detection of axions[1] in Ch.3. In Ch.4, I describe the tunable plasma haloscope concept and present our experimental setup followed by measurements and data analysis. In Ch.5, I conclude and describe future experiment trends by giving two concepts for a large-scale tunable haloscope and our laboratory's cryogenic system where we will be able to repeat and extend these measurements at temperatures at or below 4.2 K, possibly with superconducting wires.

This thesis will focus on validation of the predictions of the plasmonic behavior of the 3D metamaterial, specifically the plasma frequency and loss term (from which a quality factor may be defined) as a function of the details of the array, i.e., the wire and plane spacings, the arrangement of the planes (e.g. their relative position and angle, etc.) I find that, given the wire planes, the plasma frequency is only sensitive to the spacing of the planes, but in fact the dependence is strong, and this dependence immediately suggests a simple and practical way of accurately and reproducibly tuning the array.

The concept of the experiment is based on the Drude[2] model of solid [3, 4]. The simple metamaterial calculation of Lawson et al. [2] and the earlier fundamental models of Pendry [5] and Belov [6] are summarized in Ch.4. In terms of experiments, we first reproduce results reported by Gay-Balmaz (2002) [7] and extend them by examining the system on shift and tilt as well as different grid constellations. It is shown that with small uniform changes in wire plane spacing, the plasma frequency can be varied from 7 GHz to 14 GHz, and it is projected that a frequency of 75 GHz might be reached if an engineered frame can be assembled practically.

---

[1] The axion is a pseudoscalar, i.e., a pion-like particle with spin and parity $J^P = 0^-$.

[2] Paul Drude, German physicist, who in 1900 developed a simple model for electron conduction in metals.

Chapter 2

Introduction to Dark Matter Problem

In this chapter, I present a brief history of modern cosmology and dark matter as a major unknown component of the universe. I describe major experiments and methods of direct measurement of dark matter.

2.1 Early History of 20th Century Cosmology

By the early 20th century, the general picture of cosmology was beginning to take shape. It was realized that our Milky Way is a spiral galaxy of a large number of stars, now estimated to be 100-400 billion in number [8,9]. It was also clear that there are many galaxies in the universe beyond our own, now estimated to be about 200 billion. In 1929, Edwin Hubble published his analysis of a limited data set of galaxies for which one could measure both recession velocities (by red shift) and distance (using Cepheids variables as the standard candle) [10,11]; this confirmed the earlier predictions of Georges Lemaitre [12] who had found a self-consistent solution to Einstein's general relativistic equations for a homogeneous, matter-filled expanding universe (Fig. 1) [13].

This implied the observable universe had a beginning, which we now estimate to be approximately 13.8 Ga [14].

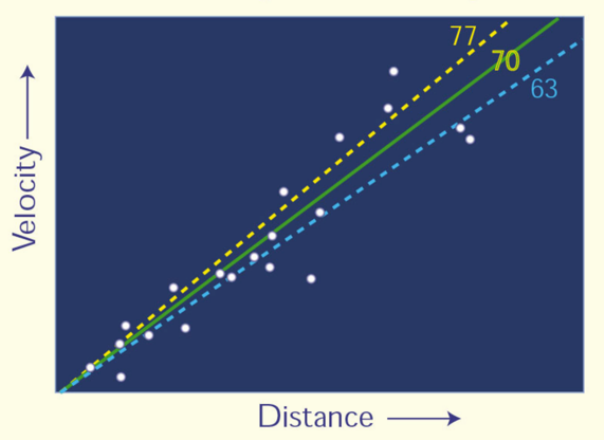

Figure 1: Hubble diagram for Cepheids variables showing galaxy distance versus the virial velocity. The slope measures Hubble constant, which quantitates the expansion rate of the universe, measures ~73 Km/s / Mpc[3].

2.2 Evidence for Dark Matter

Utilizing the same tools as Hubble, Caltech astronomer Fritz Zwicky in the 1930s determined the virial velocity of the galaxies in the Coma cluster, consisting of more than a thousand galaxies, and found it to be ~ 1000 km/sec [15]. This number was much higher than that expected based on the estimated observable mass, i.e., the purely baryonic mass associated with a standard galaxy, which led Zwicky to postulate the existence of a large unobserved component of the mass, which he termed the dark matter [64]. As galactic clusters are complicated systems, while this remained interesting speculation, there was no general acceptance of this hypothesis for three decades. In the 1960s however, Vera Rubin[4] and her collaborator William Ford measured the rotation curve of nearby galaxies and found that the tangential disk velocity remained constant, or in some cases increases, with radius as far out as there was visible light from the disk (Fig. 2) [9]. These measurements have been extended further by the use of the H I 21-centimeter line due to the electron spin-flip transition in atomic hydrogen. Spiral galaxies are a simple and clean system for which it is much more difficult to dodge the dark matter interpretation; it is easily shown that a flat rotation curve implies a total enclosed mass that grows linearly with radius; this, in turn, implies a density distribution

[3] Hubble Space Telescope, NASA Press release, May 1999.
[4] Vera Rubin, America astronomer, pioneered the research on galaxy rotation ratios.

which falls off as $1/r^2$ at large distances. The best fits to all galactic observables lead to estimates of the local dark matter density[5] of approximately 0.4 - 1.5 GeV/cm^3 [16].

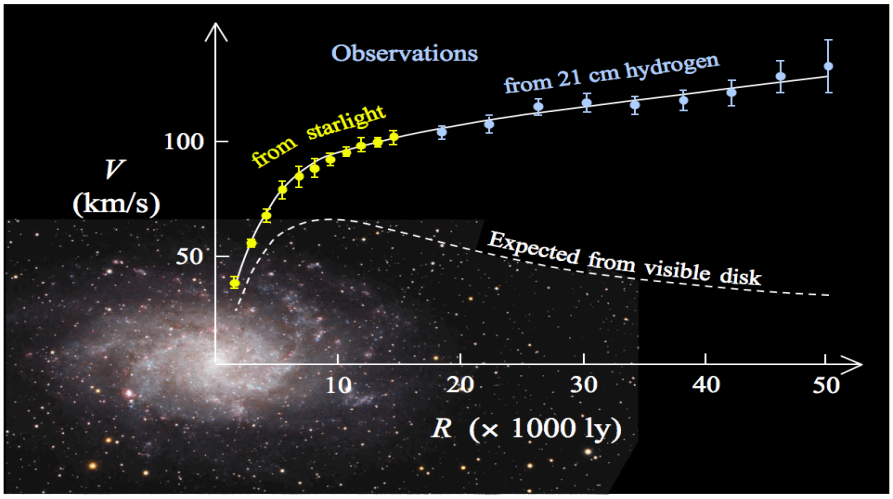

Figure 2: Rotation curves of M33 as observed in visible light and in 21-cm hydrogen line [9].

Other evidence for dark matter comes from modern estimates of the observed virial velocity of galactic clusters [17], the Cosmic Microwave Background (CMB) [18], and more indirectly from the concordance of calculations of primordial nucleosynthesis with observed light element abundances [19].

2.3 20th Century Cosmology

Two independent groups from Berkeley and Harvard, seeking to measure the Hubble diagram at large redshift z and thereby determine the total matter density of the universe, came to the surprising conclusion in 1997 that the universe was exactly closed ($\Omega = 1$) but that there was a dominant Dark Energy component to it, with all of the matter comprising only 31% of the total energy density. Dark matter is estimated to be 27%, and ordinary (Baryonic) matter[6] accounts for only 4%. While locally dark matter is very dense, ~0.45 GeV/cm^3, as it was the aggregation of dark matter that provided the gravitational potential for ordinary baryonic matter to fall into and form the structures

[5] From the Gaia satellite data. PDG.LBL. (Baudis and Profumo, 2019)
[6] Source: https://science.nasa.gov/astrophysics/focus-areas/what-is-dark-energy

that we observe today, the universe-averaged dark matter density is much more dilute, about 1.26 keV/cm^3.

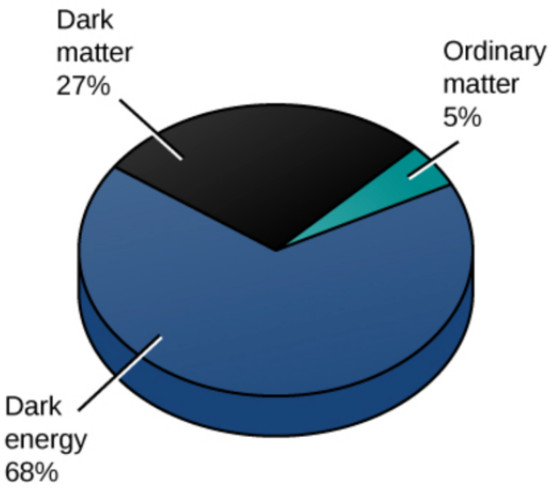

Figure 3: Composition of the universe (Image Credit: NASA).

2.4. Composition of the Dark Matter

The leading hypothesis for the dark matter is one or more species of beyond-Standard Model particles that were created abundantly at the time of the Big Bang, but whose lifetime is much greater than the lifetime of the observed universe, and whose interactions other than gravity are so weak as to have evaded detection so far.

There are two leading candidates, i.e., the WIMP (Weakly Interacting Massive Particle) and the axion, which will be discussed later. There are a variety of theoretical models, such as Supersymmetry and its extensions, which give rise to WIMPs in the early universe. There was much enthusiasm with this hypothesis initially, as the cross-section which would lead to WIMPs thermally decoupling with the proper density in the universe corresponding to the weak interaction scale, leading to it being called the "WIMP miracle".

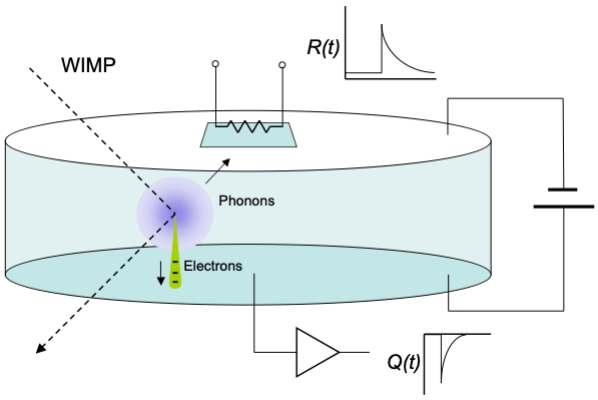

Figure 4: Schematics of single detector from CDMS experiment[7] [66].

Experiments with ultrapure solid-state germanium detectors (HPGe) (Fig. 4) or with large volumes of liquid xenon (Fig. 5) deep underground to detect the rare, low energy recoils from WIMP-nucleus collisions have been conducted, and the cross-sections for spin-independent scattering have been pushed down by many orders of magnitude and are now approaching the floor set by solar neutrinos. While next generation WIMP experiments are commissioning now, in fact, these models are currently less favored than before.

[7] Source: https://physics.aps.org/articles/v2/2

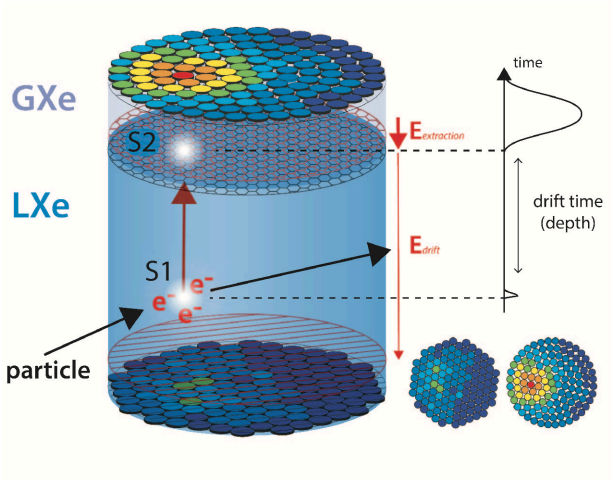

Figure 5: Schematics of XENON1T experiment[8]. The XENON1T experiment at the Laboratori Nazionali del Gran Sasso (LNGS) is the first WIMP dark matter detector operating with a liquid xenon target mass above the ton-scale [68].

[8] Source: http://www.xenon1t.org

Chapter 3

The Axion

In this chapter, I discuss the status of the axion theory and experiment with a brief introduction to the various experiments that are relevant to my research.

3.1 The Axion in Particle Physics

The previous chapter concluded with a discussion of the WIMP as a cold dark matter candidate, a very heavy particle (1-1000 times the proton mass) that would have been thermally produced during the Big Bang. Although rare (a few per cubic meter in our neighborhood of the Milky Way), it might be observable in conventional nuclear or particle physics detectors owing to its expected cross-section for nuclear scattering, i.e., within a few orders of magnitude of the weak scale ($\sigma \sim 10^{-40}$ cm^2).

Another leading candidate currently is an extremely light particle, called the axion; its mass is expected to be $m_a < 10^{-3}$ eV. Clearly, if it is to account for the local dark matter density of ~ 0.45 GeV cm^{-3}, axions at our location in the galaxy must be extremely dense, exceeding 10^{12} cm^{-3}. The axion originated as a consequence of an elegant and minimal extension of the Standard Model published by Roberto Peccei and Helen Quinn in 1977 to explain why the Strong interaction (i.e., the nuclear force) is immune from CP-violating effects when the underlying theory of the Strong interaction, Quantum Chromodynamics or QCD, seems to provide no such protection [23]. Here C and P are the Charge Conjugation and Parity operators, respectively. The most striking evidence for CP-conservation in the Strong interaction is the absence of a neutron electric dipole moment, the current limit being 1.8 x 10 $^{-26}$ e cm, some 11 orders of magnitude smaller than naive estimates of what would be expected in QCD itself. Within months of the appearance of the Peccei and Quinn paper [20], Steven Weinberg and Frank Wilczek independently realized that if the Peccei-Quinn theory was correct, their mechanism would also imply the existence of a light particle which they named the axion [21, 22].

The axion is a pseudoscalar ($J^{\pi} = 0^-$), a light cousin of the neutron pion, π^0, and as such can decay to two photons. The axion-photon coupling constant is denoted by $g_{a\gamma\gamma}$, and a property of all the axion's couplings g_{aii} (where i = leptons, quarks, nucleons,

photons) is that they are proportional to the axion's mass, m_a. Thus, very light axions interact with matter and radiation extraordinarily weakly, only gravity is being weaker.

It is remarkable to consider that while the π^0 has a lifetime of only 10^{-16} seconds, a 1 μeV axion has a lifetime of 10^{54} sec – a factor of 10^{36} longer than the age of the universe! This is the reason the axion cannot be detected by searching for a quasi-monochromatic radio line in the galactic halo of energy $E_\gamma = m_a/2$. There is an interesting irony at work here. The pion's lifetime was too short to measure accurately until Henry Primakoff conceived of a method to measure its lifetime indirectly by what is now known as the Primakoff effect [59, 64]. Now seven decades later, the axion, which is too long- lived to be observed at all, maybe rendered visible by another application of the Primakoff effect, as will be discussed below.

3.2 The Axion in Cosmology and Astrophysics

Unlike the WIMP, the axion was created as a zero-temperature field roughly a microsecond after the Big Bang and never came into thermal equilibrium with the rest of the universe. The fraction of the energy density of the universe in axions Ω_a is proportional to $(m_a)^{-7/6}$, which is why light axions are good dark matter candidates. It was thought for a long time that this provided a robust lower limit on the axion mass, as axions lighter than a few μeV would result in an overclosure problem for the universe, but recent theoretical work has found plausible mechanisms for axion generation that avoid this bound. On the upper mass end, the excellent concordance between the theoretical and observed neutrino pulse from the core-collapse (Type IIa) Supernova 1987a in the IMB and Kamiokande[9] water Cherenkov detectors and the Baksan laboratory scintillator detector[10] rules out axions between approximately 10 meV and 10 eV. This is so because, in that window, axions would have coupled so strongly to nuclear matter that they would have been created abundantly and free streamed out of the proto neutron star, foreshortening the neutrino pulse. This was not observed to happen, however, as the 25 neutrinos total were observed over a roughly 12-second window, in excellent agreement with theory, without axions [61].

A thorough discussion of the theory of the axion, its limits, and various axion detection modalities is found in a recent review [24].

---

[9] The Super-Kamiokande detector consists of a stainless-steel tank, 39.3 m diameter and 41.4 m tall, filled with 50,000 tons of ultra-pure water. 13,000 photomultipliers are installed on the tank wall.

[10] The Baksan Underground Scintillation Telescope (BUST) with a volume of 3,000 m^3. at a depth of more than 800 meters of water equivalent (m.w.e).

3.3 The Microwave Cavity Experiment

In his seminal 1983 paper [25], Pierre Sikivie realized that the axion could be detected with current technology, the experiment comprising a large superconducting magnet, a high quality-factor microwave cavity, and a state-of-the-art low noise preamplifier (Fig. 6).

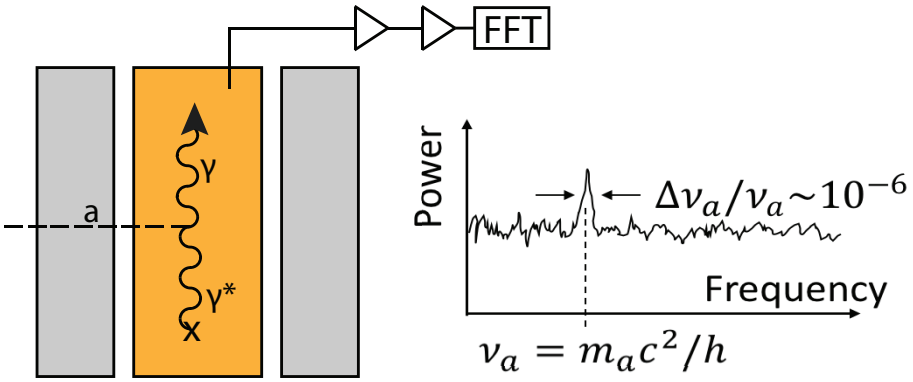

Figure 6: Simplified schematic of the microwave cavity experiment to search for dark matter axions. The superconducting magnet is indicated in grey and the microwave cavity in orange. A Fast Fourier Transform (FFT) converts the voltage-time sequence into a power spectrum within the bandpass of the cavity. The expected signal would be a small quasi-monochromatic peak of excess noise at a frequency corresponding to the mass of the axion.

The principle of the experiment is the Primakoff effect, by which a pseudoscalar, which fundamentally couples to *two* photons, may convert to a *single* real photon in the presence of an external electromagnetic field, whose energy equals the full energy (rest mass plus kinetic) of the axion (Fig. 7).

This conversion is resonantly enhanced in a microwave cavity, with the resonant condition being that $h^*\nu = m_a c^2$; numerically, 1 GHz corresponds to an axion mass of 4.126 μeV. Underpinning the experiment also is the fact that very light dark matter, with a high occupation number and large de Broglie wavelength, may be treated as a classical field.

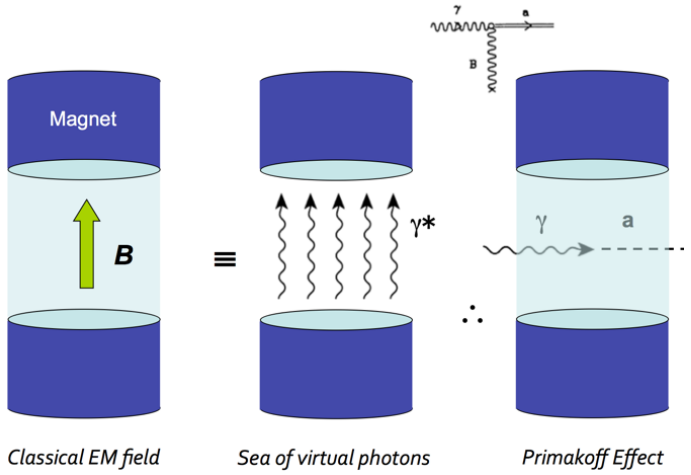

Figure 7: The Primakoff effect, by which an external electromagnetic field may be represented by a sea of virtual photons, allows a pseudoscalar, such as an axion, to scatter from this field and convert into a single real photon carrying the full energy of the axion [59].

The Conversion Power

The power relation is then determined by the magnetic field and the volume of the cavity, as well as the Q-factor, following the equation:

$$P_{sig} \propto \{\frac{g^2}{m_a^2}\rho_{DM}\} * \{B^2\ V\ \mathrm{C}\ Q\ \omega_c\}$$

where P_{sig} is the signal power in Watt. The first term in parenthesis is determined by astrophysical parameters, where g^2 is the axion-photon coupling constant, m_a is the axion mass, and ρ_{DM} is the dark matter density in the galactic halo. The second term in parenthesis is determined by experimental parameters, where B is the magnetic field, V is the volume of the cavity, C is the form factor, which describes the overlap of the axion-induced electric field E, with the external magnetic field B; ω_c is the resonance frequency of the cavity. Q is the quality factor that is determined by Γ and it is defined as the ratio of stored energy U to the dissipated power of the system P_{diss}:

$$Q = \omega_c \frac{U}{P_{diss}}$$

where ω_c is the resonance mode frequency.

As the quality factor Q ~ $10^{4\text{-}5}$ whereas the effective Q of the axion, Q_a ~ 10^6, the axion signal would appear as a narrow Maxwellian peak of excess noise on a broader Lorentzian background. As the axion mass and thus frequency is not known, the cavity must be tuned in very small overlapping steps of the cavity bandwidth, integrating for times of minutes to hours at each frequency.

In this scheme, the axion a interacts with a virtual photon γ^* in the magnetic field to convert to a full energy photon γ. This phenomenon occurs when the axion mass matches the resonance frequency of the cavity.

As mentioned previously, the allowed mass range of the axion covers from μeV to meV, or roughly MHz to THz, although the region of 3.4-8.8 GHz is of particular interest according to recent calculations by Klaer and Moore [26] and Safdi [27], nicely within the range of the HAYSTAC experiment. While there are many challenges for the microwave cavity axion experiment, a good fraction of them involves the microwave cavity itself.

A suitable cavity for the experiment must satisfy multiple simultaneous criteria. (i.) It should have as large a volume as possible, as the conversion power is proportional to V. (ii.) The quality factor Q should be as large as possible, as the conversion power is likewise proportional to it. Cavities entirely made of superconducting material are not feasible, as the cavity resides in a magnetic field upward of 10 T. (iii.) The cavity should possess a good form factor, C_{nlm}, ideally ~ *O* (1), as the power conversion is linearly dependent on this factor as well. The form factor is defined as:

$$C_{mnp} = \frac{\left(\int \vec{E} \cdot \vec{B}_0 \, dV\right)^2}{B_0^2 V \int \epsilon_r E^2 \, dV} = \frac{\left(\int E_z B_0 \, dV\right)^2}{B_0^2 V \int E^2 \, dV} = \frac{\left(\int E_z \, dV\right)^2}{V \int E^2 \, dV} = \frac{2\pi L \int_0^{R_{\text{cav}}} E_z(r) r \, dr}{V 2\pi L \int_0^{R_{\text{cav}}} E(r)^2 r \, dr}$$

and as can be seen, it is dependent on the square of the overlap integral between the external magnetic field, almost always a uniform magnetic field of strength B_0, and the cavity mode, which is read out. For the case of a uniform magnetic field, the mode with the largest form factor is the TM_{010} mode, with the higher transverse magnetic modes TM_{0n0} falling off rapidly with higher n. The form factor for all TE and TEM modes in cylindrical cavities is identically zero. For the TM_{010} mode and an empty cylindrical cavity, the frequency is given by f [GHz] = 0.115 / R [m], where R is the radius of the cavity. The frequency can be raised significantly by the insertion of a metal tuning rod into the cavity and tuned by offsetting the rod radially, but there are other tuning schemes as well.

Additionally, (iv.) the cavity must be fabricated with high precision, as even small non-uniformities in machining, misalignment of the tuning rod, etc. can cause mode localization, which will lead to degradation of the form factor C. (v.) The cavity should be tunable over a wide dynamic range. Finally, (vi.) from a practical standpoint, cylindrical cavities should adhere to an aspect ratio that is not too extreme; most experiments to date have utilized cavities with a height to diameter ratio of (2-3):1. The problem is that as the mode of interest, normally the TM_{010} mode is tuned in frequency by radially offsetting a metal or dielectric tuning rod, it encounters and mixes with a forest of TE modes, and at each mode-crossing (completely analogous to two-mode mixing in quantum mechanics) leading to a notch in frequency coverage which is lost. Fig. 8 shows the cavity used by the Yale-Berkeley-Colorado HAYSTAC[11] experiment; this cavity is annealed electroplated copper on a stainless-steel body, of length of 25 cm and 10 cm diameter. The Q at cryogenic temperatures is typically 40,000 [28].

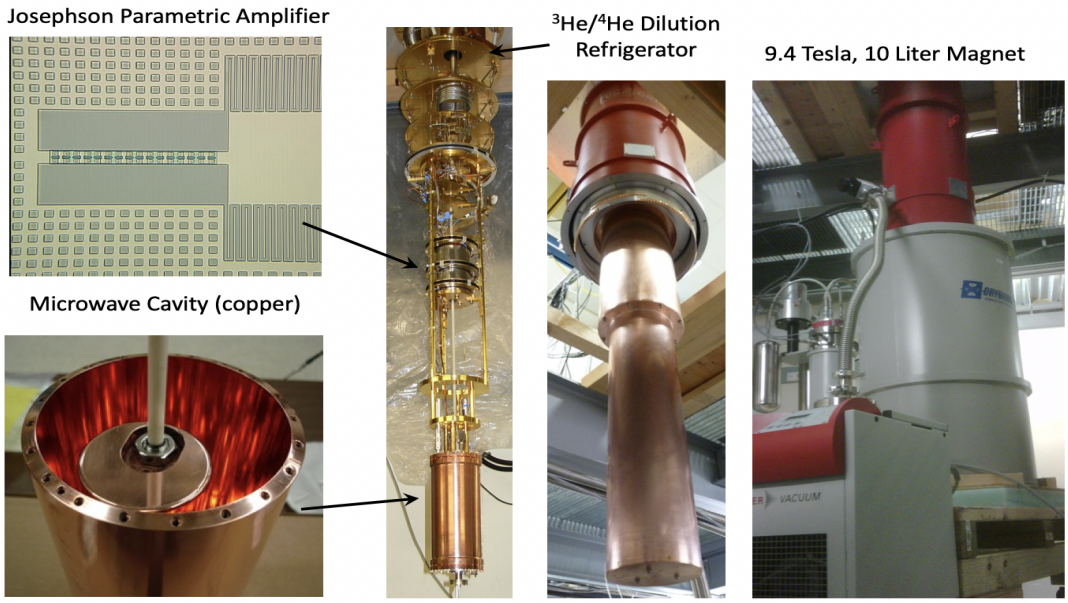

Figure 8: Laboratory setup of HAYSTAC experiment.

However, putting all together (i.) maximizing the volume, while (iii.) maximizing the form factor, yet (iv.) keeping to a low aspect ratio leads to a problem that traditional

[11] The Haloscope at Yale Sensitive to Axion CDM (HAYSTAC) is a tunable microwave cavity experiment searching for axion dark matter in the galactic halo. The present configuration of the experiment has taken data at various frequencies within the 3.4-5.8 GHz range (14-24 μeV), but for which extensions are being planned to ~12 GHz (50 μeV). (https://haystac.yale.edu).

cavities become unrealizable much above 10 GHz; the fundamental difficulty is that the volume of higher frequency cavities falls as $V \sim f^{-3}$. There are new developments in the application of Photonic Band Gap resonators, which can totally eliminate the forest of TE and TEM modes [59] and tunable multi-rod cavities, which can extend the usable range of large cavities upwards to 10-12 GHz with good figure-of-merit [28], but how to build a haloscope for axions of 30 or 100 GHz remains an open problem. This is the motivation for this thesis, and which will be described in Chapters 4 and 5.

3.4 Status of the Microwave Cavity Axion Experiment

Since the pioneering experiments of the Rochester-Brookhaven-Fermilab collaboration [61], and the University of Florida [63] in the late 1980s, several groups have performed larger and more advanced searches [62]. Notable among them have been the ADMX collaboration, which represented a large-scale-up in magnet volume [29], the CAPP experiment in Korea [30], and the HAYSTAC experiment of which our group is one of the three founding institutions. HAYSTAC has pioneered the use of quantum-limited amplifiers (Josephson Parametric Amplifiers, or JPAs), which enabled the experiment to take data within a factor of two of the Standard Quantum Limit and is still the only experiment to come within an order of magnitude of it [31].

Recently, HAYSTAC has deployed a squeezed-vacuum state receiver which circumvents the Standard Quantum Limit entirely, and this work has been published in *Nature* [32] (Fig. 9).

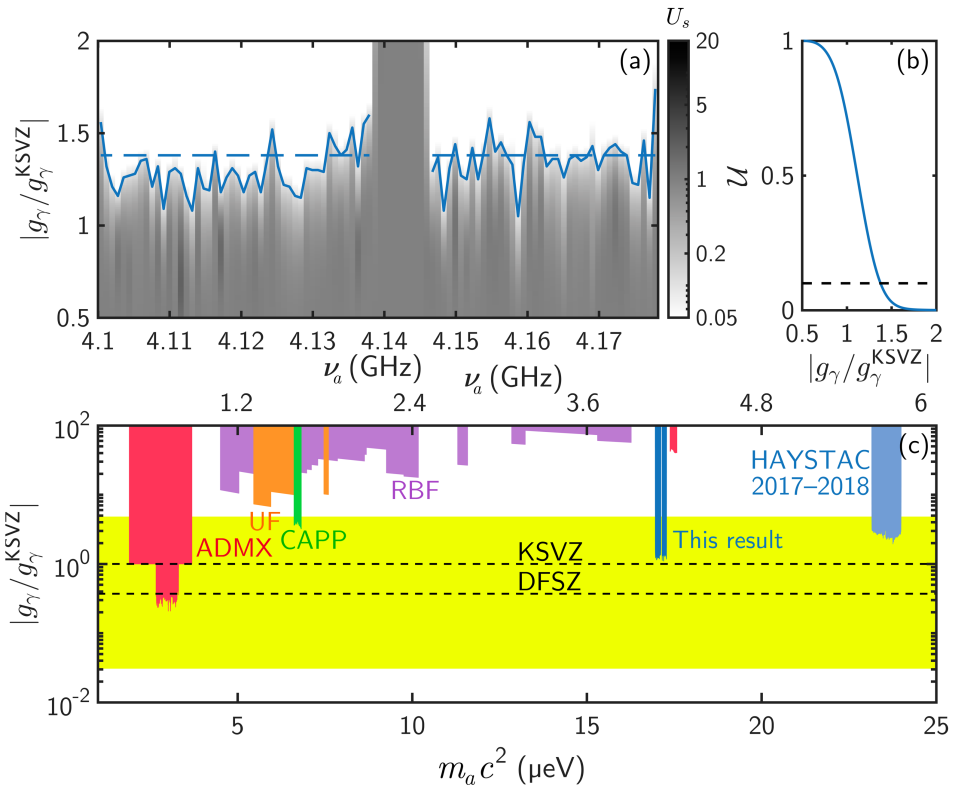

Figure 9: Regions of the axion parameter space (mass, photon coupling) excluded by HAYSTAC and other microwave cavity dark matter axion searches (Backes et al., 2021) [32].

It is the first and only quantum-enhanced dark matter experiment to date and with LIGO, one of only two experiments to utilize squeezed states in improving the sensitivity of a fundamental science experiment.

The ultimate reach in the sensitivity of a microwave cavity axion experiment, as with many other experiments of a similar nature, does not depend solely on the signal power but also dramatic noise reduction to achieve a signal-to-noise ratio enabling discovery. We have only touched upon the topic of amplifiers, receivers, and noise, as the focus of this research is solely on developing a strategy to extend the mass reach upwards.

Chapter 4

The Tunable Plasma Haloscope

In the previous chapter, the principle of the microwave cavity axion experiment was presented, and a summary of results to date; it concluded with a discussion of its principles drawback, i.e., its practical limitation in reaching higher masses owing to the highly unfavorable scaling of cavity volume with frequency. In this chapter, I describe a new implementation of the Primakoff effect for axion detection, recently published, which circumvents this limitation, the tunable plasma haloscope. Specifically, the physics application will first be reviewed, followed by the fundamentals of 3D wire metamaterials and predictions for the plasma frequency of such arrays. Finally, the chapter concludes with experimental tests of these results conducted at Berkeley will be presented, including exploration of various schemes to tune the plasma frequency over a wide dynamic range in a practical way.

4.1 Tunable Plasma Haloscope Concept

The essence of the problem with extending the microwave cavity experiment to higher frequencies, and in particular beyond about 10 GHz, is that the size of the cavity is related linearly to the wavelength of the electromagnetic mode, which is inversely proportional to the frequency; the relationship is not perfectly identical of course. Unlike a wave in free space, the electromagnetic mode in a microwave cavity must satisfy boundary conditions, in particular, that the parallel component of the electric field vanishes on the wall. For the TM_{010} mode in a right circular cavity, for example, the cavity diameter is given by

$$D[m] = \frac{0.23}{f[GHz]}$$

whereas the wavelength in free space is given by

$$\lambda[m] = \frac{0.30}{f[GHz]}$$

or alternatively that the cavity diameter is 50% larger than the half-wavelength of the free-space wave.

The kernel of the idea of the tunable plasmonic haloscope is to observe that in the case of cold plasma, the dispersion relationship is given by

$$\omega^2 = \omega_p^2 + c^2 k^2$$

where $\omega = 2\pi f$, the plasma frequency is designated by ω_p, and the wavenumber is given by $k = \frac{2\pi}{\lambda}$. Thus, for frequencies just above the cutoff, i.e., $\omega \gtrsim \omega_p$, the wavelength λ can be arbitrarily large. This suggests a strategy for the design of a Primakoff-based dark matter axion experiment based on cold plasma. Contemplating the use of ionized gas plasma, of course, raises some immediate questions, most particularly its temperature; even plasmas described as 'cold' (in lab contexts or astrophysical contexts) are typically still hotter by some orders of magnitude than the temperatures desired to reduce the blackbody photon noise to levels where the minuscule axion signal may be observed (the HAYSTAC experiment, for example, operates at a temperature of ~100 mK). How one would control the free electron density to set the plasma frequency to the desired value is another issue. In addition that plasmas are intrinsically lossy, which represents an impediment to achieving a suitable equivalent quality factor *Q*, necessary to allow the conversion signal to build up.

There are systems, however, which are well described as plasmas and thus may represent useful surrogates for the application to the Primakoff-based dark matter axion search. A recent proposal is given by Lawson et al. and involves a 3D wire array metamaterial [2]. Likewise, the free carriers in a semiconductor represent another plausible realization of the idea, which is also under study by the same Stockholm group. This thesis focuses solely on the 3D metamaterial approach, and which was specifically proposed to us by the Stockholm group, who were looking for an experimental partner to collaborate with them and carry out the R&D based on their theoretical work.

The Lawson et al. [2] report begins by incorporating the axion into Maxwell's equations in the usual way, which assumes that the axion can be treated simply as a spatially constant classical field, i.e., has a very high occupation number, and long de Broglie wavelength:

$$\boldsymbol{\nabla} \times \mathbf{H} - \dot{\mathbf{D}} = g_{a\gamma} \mathbf{B}_{\mathrm{e}} \dot{a}$$

where B_e represents the external magnetic field, and the axion field $a(t) = a_0 e^{-i\omega_a t}$.

The oscillating axion field thus acts as an effective current, driving the system at an angular frequency ω_a.

If we solve the equation above for an infinite medium of dielectric constant ε and utilize a Drude model [3] for the dielectric constant, we have

$$\mathbf{E} = -\frac{g_{a\gamma}\mathbf{B}_e a}{\epsilon} = -g_{a\gamma}\mathbf{B}_e a\left(1 - \frac{\omega_p^2}{\omega_a^2 - i\omega_a\Gamma}\right)^{-1}$$

where ω_p is the plasma frequency and Γ the damping rate, which sets the plasmon lifetime, when the plasma frequency matches the axion frequency. Note that when the damping is small, the system possesses a resonance corresponding to matching the plasma frequency to the axion frequency, $\omega_p = \omega_a$. Note that the resonance frequency does not depend on the size of the system but is rather a property of the medium.

Lawson et al. [2] calculate the response of a finite homogeneous plasma, both analytically and by simulation, where the agreement with one another is essentially perfect and bear out the expected behavior.

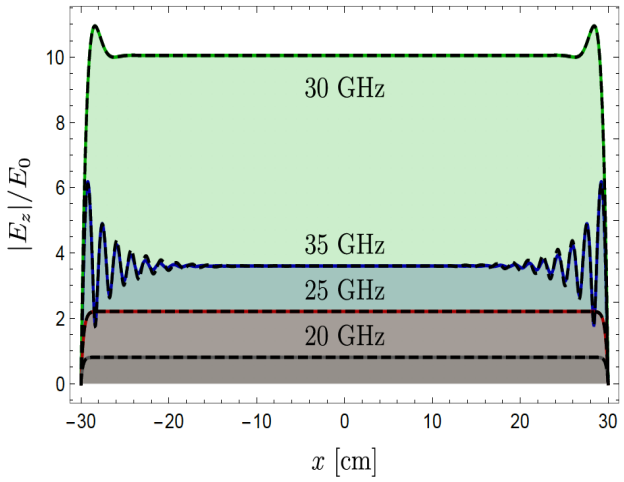

Figure 10: Analytic and numerical calculations of the E-field as a function of radius in a plasma cylinder of 30 cm radius and 2.7 m in height. The plasma angular frequency was chosen to be ω_p = 30 GHz, and the response of the plasma was calculated for an axion angular frequency of 20, 25, 30, and 35 GHz. In this example, the damping was chosen to be $\Gamma = 10^{-1} \times \omega_p$. The black dashed lines represent the numerical calculations performed in COMSOL, and the colored lines represent the analytic calculations [2]. The agreement is excellent.

4.2 Wire Array Metamaterials

As mentioned previously, this thesis focuses on the possible utility of wire metamaterials as a plasma surrogate which may prove practical for use in a dark matter axion experiment. Exactly what constitutes 'practical' will be discussed further on, but two criteria are clear; first, that the system is tunable in a precise and reproducible way, and second that it should be able to be cooled down to cryogenic temperatures for noise reduction. Wire arrays can plausibly meet these conditions.

Metamaterials based on 3D wire arrays were actively studied two decades ago, and there is a well-developed theory describing them. It considers a homogeneous array of thin wires aligned in the z-direction of radius r and spacing a [5]. If the wires are sufficiently thin ($\ln\left(\frac{a}{r}\right) \gg 1$), they act as an effective medium with a dielectric constant given by:

$$\epsilon_z = 1 - \frac{\omega_p^2}{\omega^2 - k_z^2 + i\omega\Gamma}$$

and if $k_z = 0$, i.e., the axion velocity can be neglected, then the expression reduces to a simple Drude-like model.

The plasma frequency in bulk metals is characteristically in the PHz regime (10^{15} sec^{-1}), which thus raises the question of how could a wire array metamaterial have a usefully much lower plasma frequency (10-100 GHz or perhaps higher). Two factors in the description of the wire-array metamaterial provide the answer. First, the average electron density is much smaller, as the average electron density is greatly reduced compared to bulk metals:

$$n_e = n\frac{\pi r^2}{a^2}$$

Second, the inductance of the wires modifies the effective electron mass m_{eff}:

$$m_{eff} = \frac{e^2\pi r^2 n}{2\pi}\log\frac{a}{r}$$

Then solving for plasma frequency, ω_p, the result is:

$$\omega_p^2 = \frac{n_e e^2}{m_{eff}} = \frac{2\pi}{a^2\log(a/r)}$$

where clearly the formula is expressed in the shorthand of high energy physics where the fundamental constants are set equal to unity (here c = 1) for convenience of algebraic manipulation, and only reinserted at the end for numerical evaluation; it is always obvious by the units what needs to be reinserted. A more basic question may suggest itself, i.e., why in calculating the average electron density, do Pendry et al. [5] calculate the array-averaged electron density using the full cross-sectional area of the wire (which will be tens of microns in radius) when the electrical currents in the wire will be localized to a skin depth much less than that (a fraction of a micron in the 10 GHz range)? While that is true, it should be noticed that in the formula for the plasma frequency above, the effective mass in the denominator contains the exact same factor $\pi r^2 n$, and thus cancels out, leaving the expression for the plasma frequency, which is independent of the bulk electron density, and independent of the wire radius r as well, except weakly through the logarithmic term.

While detailed numerical evaluations will be presented further on, as a simple example, if r = 25 μm, and a = 5 mm, then the logarithmic term $\ln\left(\frac{a}{r}\right) \approx 5.3$, so the condition on the validity of the treatment is well satisfied, and the plasma frequency $f_p = (2\pi)^{-1}\omega_p$ ~ 7.35 GHz, six orders of magnitude lower than the plasma frequency in bulk metal. A highly schematic realization of the plasmon-axion resonator is presented in Fig. 11.

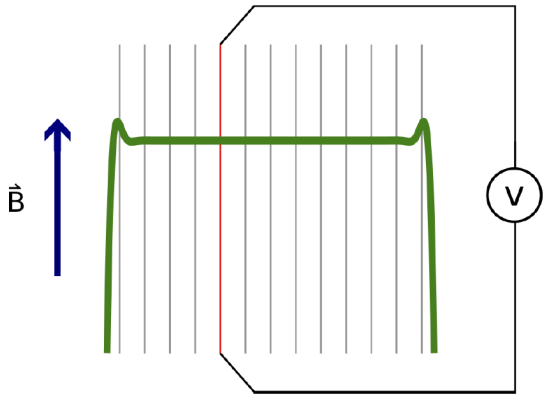

Figure 11: Conceptualization of a plasmonic resonator to detect dark matter axions (Lawson et al., 2019) [2]. A strong magnetic field is applied parallel to the wire array. In Lawson et al., it is suggested coupling the preamplifier to one of the wires in the array as the signal readout; however, it is far from clear that such a scheme would be successful, owing to the very short Compton wavelength of the axion being sought. The readout scheme is one of the significant outstanding issues of this scheme, and while we present a notional readout scheme later, a solution to this problem is not within the scope of this thesis.

4.3 Modeling of Metamaterial Array

This chapter concludes with an evaluation of the plasma frequency for various choices of parameters (i.e., wire diameter and spacing) which could be readily fabricated and tested to compare with the limited cases that have been calculated and published. The actual experiments and data will be the subject of the following chapter.

The first and simplest case to be worked out is an approximate analytical treatment of Pendry et al. [5], previously cited, for a square array of wires, of radius r and spacing a:

$$\omega_p^2 = \frac{n_{\text{eff}} e^2}{\varepsilon_0 m_{\text{eff}}} = \frac{2\pi c_0^2}{a^2 \ln(a/r)}$$

I analyze the effect of wire diameter as a function of frequency, as shown in Fig. 12. The frequency will increase with a decrease in wire diameter. At the same time, the wire spacing is significantly more efficient when it comes to achieving higher frequencies. I can achieve >10 GHz at spacing below 5 mm in a square grid with any wire radius < 100 microns.

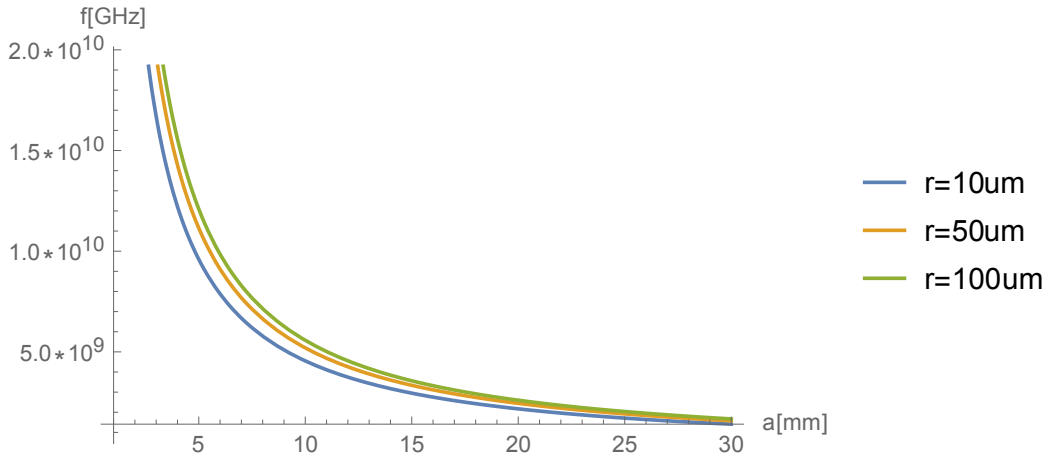

Figure 12: Plasma frequency as a function of wire spacing and diameter for the approximate analytical treatment of Pendry et al. [5].

The analysis above is limited to the spacing between wires in a square grid. However, Belov et al. has derived an improved general solution for a rectangular wire grid for the case of wire spacing a, b [6].

The generalized equation now takes the form

$$k_0^2 = \frac{\frac{2\pi}{s^2}}{ln\frac{s}{2\pi r_0} + F(r)}$$

where $s = \sqrt{ab}$, r = a/b, r_0 = wire radius, and $\omega_0 = k_0 \frac{1}{\sqrt{\varepsilon_0 \mu_0}}$.

The function F(r) can be calculated analytically as an infinite sum that is equal to 0.5275 for the case of the ratio r = a/b= 1, i.e., a square lattice. Clearly this function must satisfy the condition F(r) = F(1/r). Fig. 13 shows a plot of the function F(r) for a rectangular array. when r goes larger, F(r) is close to $\frac{\pi}{6}$ - $\frac{1}{2}$ ln r.

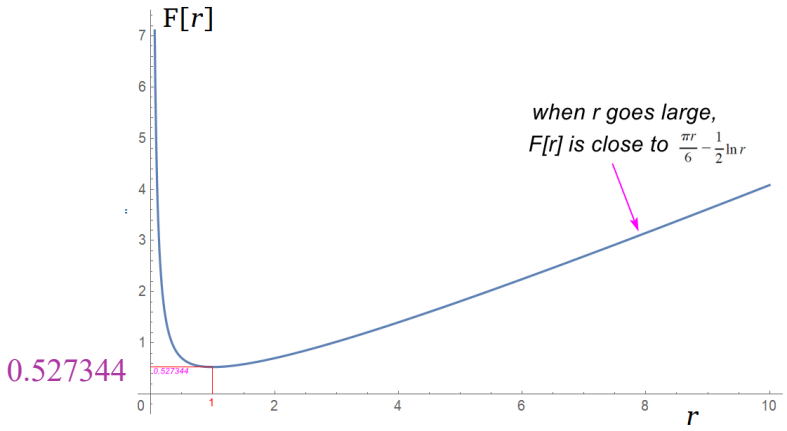

Figure 13: Plot of the function F(r) in Belov et al. for the case of a rectangular array of thin wires, where a is the spacings of the wires, b is the spacing between the planes, and r = a/b.

If one compares the computed results from Pendry et al. [5] and Belov et al. [6] for the case of a square lattice, it is evident that there is a discrepancy in the denominator, leading to a small (order of 10%) difference in wire spacing to achieve the desired frequency. The computed results of both equations are shown in Table 1.

Frequency	a [Pendry]	a [Belov]
8 GHz	5.9 mm	6.57 mm
10 GHz	4.8 mm	5.36 mm
12 GHz	4.0 mm	4.54 mm
15 GHz	3.3 mm	3.71 mm
18 GHz	2.8 mm	3.15 mm

Table 1 Comparison of wire spacing as suggested in Pendry and Belov equations for the case of a square lattice [5, 6].

As will be seen in the next chapter, these values suggest that the metamaterial haloscope concept can be readily tested in the 10 GHz range with stacks of wire planes similar to those used in high energy physics, i.e., wires of tens of microns, with few millimeters spacing.

Chapter 5

Experimental Tests of Wire Array Metamaterials

In this chapter, I present the plans of the experiments, define the variables, and describe the setting of the experiments. Then, I present the measurements and how the data was acquired by describing the hardware designed and implemented in the experiments. Least-squares fitting was applied to extract quantities of interest from each measurement and thus to further develop the phenomenology of wire area metamaterials. A comparison with computed theoretical equations, measured data values, and fitting to the mathematical model is presented, followed by research conclusions.

5.1 Introduction

The purpose of the experimental program in this research is to validate the theory of 3D wire array metamaterials and extend the measurements to designs of arrays where there are currently no theoretical predictions. The ultimate goal of the experimental program is to identify the most promising engineering implementation(s) that will satisfy all the requirements and desirable features of such an array for use in a large-scale axion experiment. Primarily these are ease and cost of fabrication, ability to deploy in meter-scale size, a method for tuning the array over a wide dynamic range in frequency that is precise, reproducible, and simple, extendable to 30 GHz and above, a high quality-factor Q, and being easily cooled to cryogenic temperatures. This thesis will focus mostly on validating the theoretical calculations and determining a robust tuning scheme but will also present a conceptual design for a large-scale experiment.

While there are multiple ways of creating a 3D wire array for this program, the most compelling option is to create the array from planes of wires on thin frames and stack them together. It is attractive both because there is a large experience base going back decades from making large area planes of thin (radius 20-50 μm) gold-coated tungsten wires with mm-scale spacing for high energy physics detectors [66], and also because assembling the 3D array from discrete planes gives us many degrees of freedom for changing the configuration of the array.

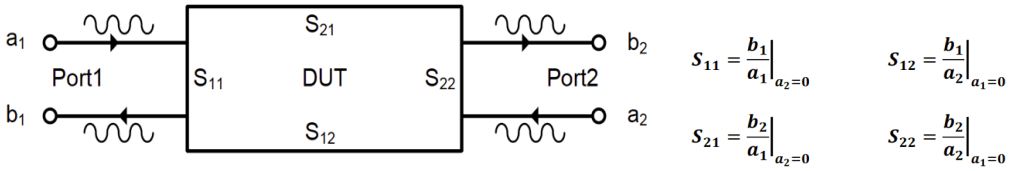

Figure 14: Definition of the microwave S-Parameters for Device Under Test (DUT)[12]. We measure S_{21}, which is the ratio of the energy output of the system to the energy input due to attenuation inside the system. No reflection or scattering is included in this study.

The primary method for testing the plasmonic response of the 3D wire array is to do microwave transmission measurements through the array, measuring what is termed the S_{21} parameters. As will be seen, the amplitude and phase of the transmitted wave as a function of frequency encodes both the plasma frequency ω_p and the loss, Γ from which one can define a quality factor analogous to that of the microwave cavity, $Q = \omega_p / \Gamma$.

5.2 Wire Frame Design and Construction

As mentioned, assembling and arranging discrete planes of wires was deemed the most practical approach to explore the plasmonic behavior of 3D wire arrays. In this section, I describe the design, fabrication, and mechanical assembly.

The S_{21} measurements, described in more detail later, consists of transmitting a swept microwave tone transversely through the 3D wire array consisting of stacked planes, where in general, the orientation of the wires ($\hat{z}$) aligns with the polarization of the microwave signal (although tests will be done later where this is violated). Given the microwave horns selected for transmission and reception of the signal, the frames were chosen just large enough to be safely outside of the direct beam, so reflections from the frames would only contribute negligibly to the problem. The planes were square 10" on a side, with 8.00" square cut out of them. (Fig. 15).

For stiffness and maintaining planarity, stainless steel was selected as the material. Holes of 0.250" were drilled in the four corners of the frames so that they could be

[12] Keysight Technologies: "S-Parameter Measurements Basics for High-Speed Digital Engineers". www.keysight.com

assembled on 0.250" threaded nylon rods, which provided both accurate plane-to-plane registration and an easy way of changing the interplane spacing by the introduction of spacers.

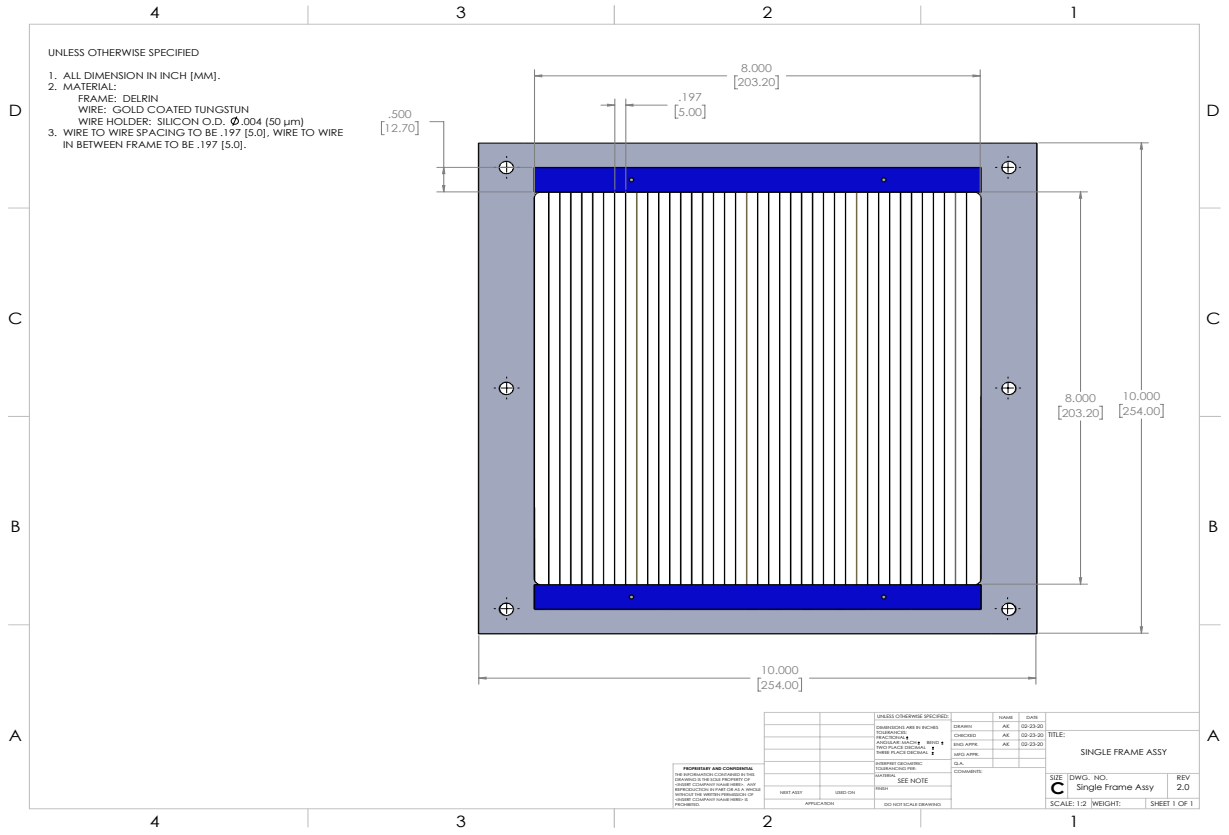

Figure 15: CAD drawing of the wire frame of a square design, fabricated of 1.7 mm stainless steel sheets. The aperture window of 8"x8" was chosen to be safely larger than the microwave horns (5" x 3.7").

The ideal wire should be strong but very thin and highly conductive. The latter condition is synonymous with having as small a skin depth as possible for normal conducting wires. The classical skin depth[13], which pertains at room temperatures [Fig. 16], is given by:

$$\delta = \sqrt{\frac{\rho}{\pi f_o \mu_r \mu_o}}$$

[13] Jackson, Classical Electrodynamics, p. 220.

where ρ is the bulk resistivity in metal in Ω·m, f_0 is the frequency, and μ_0, μ_r is the permeability of free space, and the relative permeability, respectively. It is important to note that δ decreases with higher frequency. The resistivity for gold (Au) is 2.349×10^{-8} Ω·m, and μ_0 equal $4\pi \cdot 10^{-7}$ H/m, will give us δ = 0.77 μm at a frequency of 10 GHz[14].

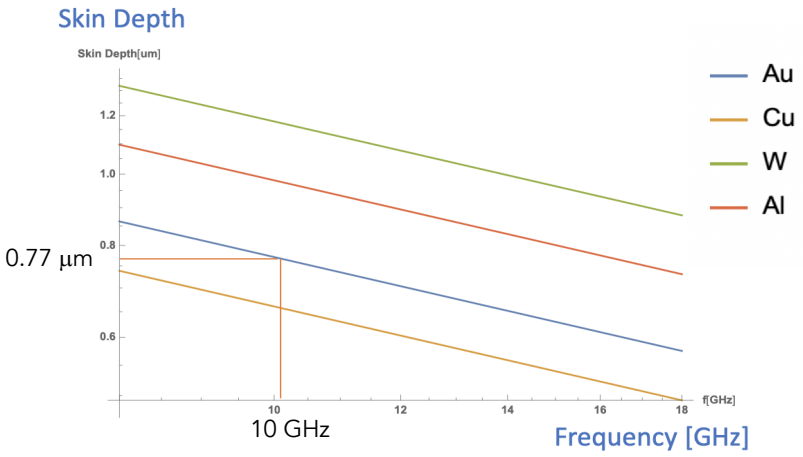

Figure 16: Skin depth of some common candidate metals as a function of frequency.

Unfortunately, the highest conductivity metals are also among the most malleable, which would imply that very thin wires made of these metals would plastically deform (stretch) under tension and sag, rendering them unsatisfactory for use in planes. However, some fifty years ago, the multiple wire proportional chamber was developed as a practical and scalable technology for particle tracking in large detectors, which have nearly identical requirements as our case, i.e., very thin wires (order of tens of microns), spaced by a few millimeters, and put under tension over spans of several meters. This application drove a large market for gold-coated tungsten wires, which combine the virtues of good conductivity and high strength. We thus chose 50 μm gold-coated wires, which we procured from Luma Metall[15]. The spacing between wires was chosen to be 5.38 mm to achieve a plasma frequency of approximately 10 GHz for a square array. In this way, each frame supports 38 parallel wires.

A wire assembly station was built to align the wires in position within each frame to assure precise localization and tension of the parallel wires, as displayed in Fig. 17. It was unclear at the outset whether it was necessary for the wires to float, i.e., remain

[14] The gold-coating on tungsten wires is 0.5 micron, means that part of the wave is traveling through the tungsten.

[15] Luma Metall AB, Kalmar, Sweden (https://luma-metall.com).

electrically isolated from their frames, or whether allowing the wires to be in electrical contact with the frame would have no effect on the plasmonic response of the array.

The decision was made to string the frames such that the wires would float, and thus nylon strips were first affixed to the frame to serve as an insulator between the wires and the metallic frame. After stretching the wires over the frame, they were bonded to the strip with a silicon-based epoxy. Finally, the wires were additionally covered with a strip of Kapton tape to prevent any accidental conduction between them and an adjacent frame.

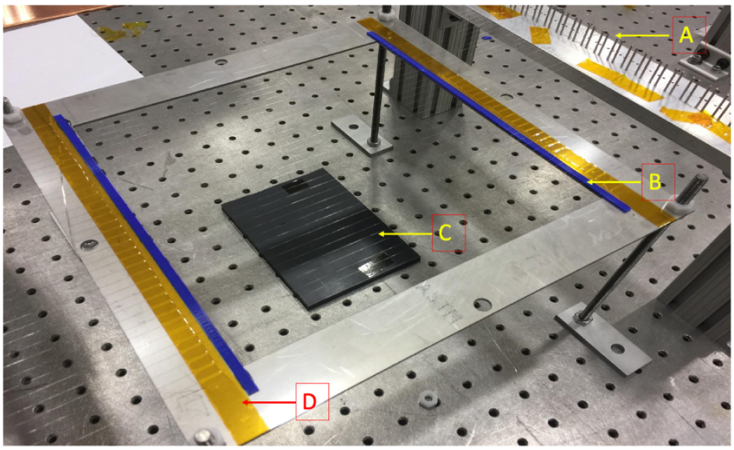

Figure 17: Assembly and alignment station: A) alignment pins; B) nylon pad; C) gold-coated tungsten wires; and D) Kapton tape strips.

Twenty frames were fabricated and ready for use at any given time, and this was the maximum number that was assembled into an array for our measurements. In fact, the overall experimental campaign required making many more due to frequent unavoidable damage to the wires during experimentation.

The frames are always oriented perpendicular to the optical table, i.e., vertically, and thus they are stacked horizontally into the array. Threaded nylon rods of 0.250" diameter is used to mount the frames, which are separated by nylon spacers of varying number depending on the test being performed. The frames are pinned to the holding fixtures on four locations and relative to each other on additional four locations.

5.3 Outline and Mechanical Description of the Measurement Program

The purpose of the program of measurements is to validate the basic theory of 3D wire array metamaterials and explore excursions in various parameters of the array with a view to determining the most practical scheme for tuning it over a wide dynamic range in frequency. For the first part, we will perform some measurements that have been done and published already and with similar parameters (i.e., wire diameter and spacing), but then extend these measurements, specifically to higher aspect ratios of wire spacings, a/b. For the second part, we will explore two other degrees of freedom where there are no detailed theoretical predictions.

Thus, the program will comprise:

1. Square lattice arrays (b = a): N (number of frames) as the variable,

2. Parallelogram arrays: x (relative translation of odd, even sets of interdigitated planes),

3. Rectangular lattice arrays (b ≠ a): b, the spacing between frames as the variable,

4. Rotated arrays: Rotation of odd, even sets of interdigitated planes by $\pm\theta$ relative to the polarization axis of the microwave signal: the angle θ is the variable.

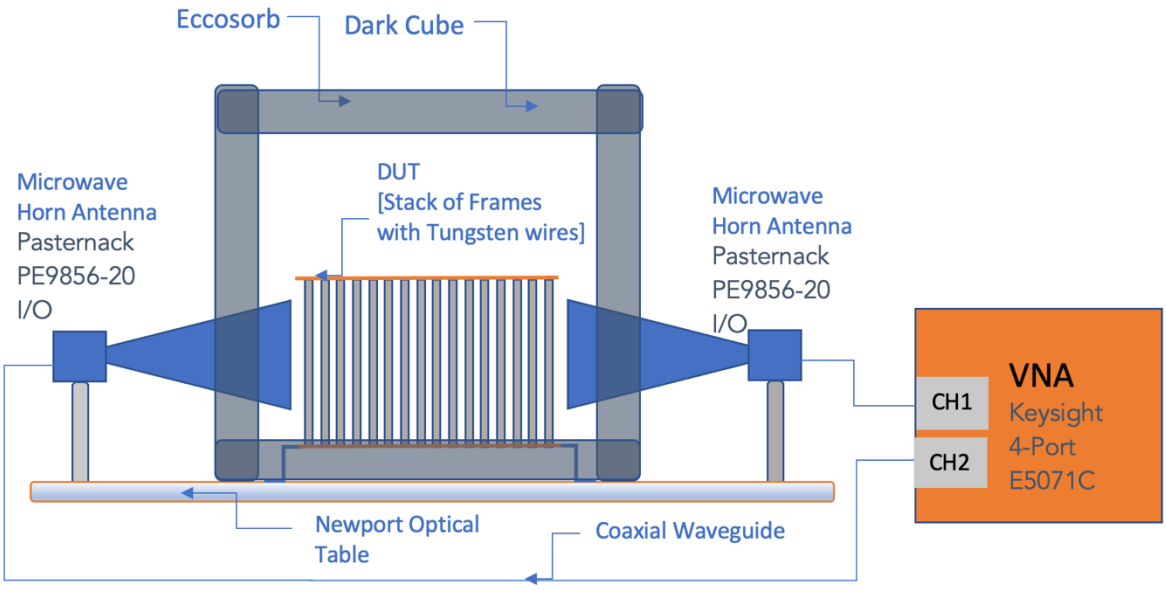

Figure 18: Schematic of the S_{21} measurements with two horn antennas.

The S_{21} measurements are performed as depicted in the schematic in Fig. 18. A photograph with the actual setup of the experiment is shown in Fig. 19.

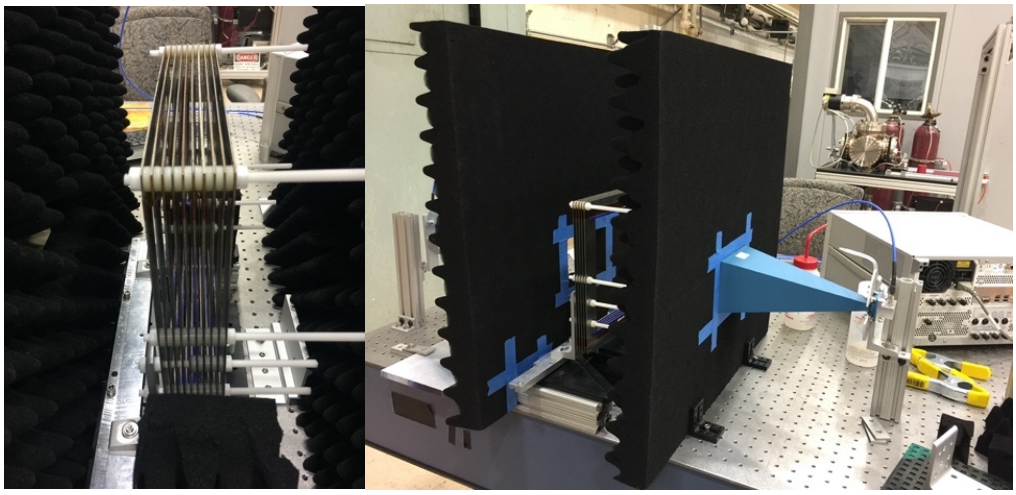

Figure 19: Photograph of a partially assembled array with 10 frames stacked together.

Electronic Hardware

The Pasternack PE9856-20 WR-90[16] standard gain horn antenna has a 20 dB nominal gain with a minimum frequency of 8.2 GHz and a maximum frequency of 12.4 GHz. It has a vertical beamwidth of 16.5° and a horizontal beamwidth of 16.1° at 3 dB.

The Vector Network Analyzer (VNA) used for all our measurements is a Keysight 4-Port E5071C with a frequency range from 300 kHz to 20 GHz. Before each measurement, the VNA underwent a five-minute calibration procedure utilizing an Agilent N4691-60004 Electronic Calibration Module.

For accurate, reproducible results, it is important that the two cables from the VNA to the transmitter and receiver horns have as little bend in them as possible, that is to say, as large a radius of curvature everywhere and that the cables are not moved once a run or series of runs have begun.

Dark Cube™

In order to achieve high quality measurement, I designed a cube of Eccosorb[17] panels that completely surround the assembly of the detector with aperture windows that fits the horn antenna's ends, namely 5"x 3.7". All measurements are taken inside the cube. Fig. 21 shows the reflectivity as a function of frequency for the measurement interval of 7 to 12 GHz.

[16] See data sheet in Appendix B.

[17] Eccosorb by MAST Technologies: (https://www.masttechnologies.com/products/commercial/rf-absorbers-commercial/convoluted-foam-3-0/).

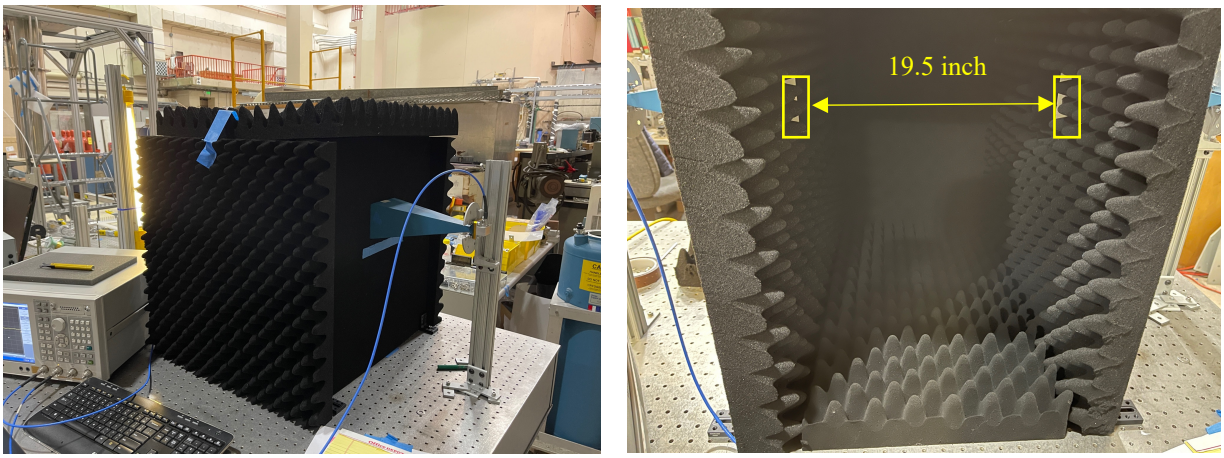

Figure 20: Dark Cube is constructed of 24" x 24" x 24" cube of Eccosorb convoluted foam panels to prevent microwave EM-interference. Openings on opposite sides define the aperture of the experiment. The quality of the measurement drastically improved when implementing the cube.

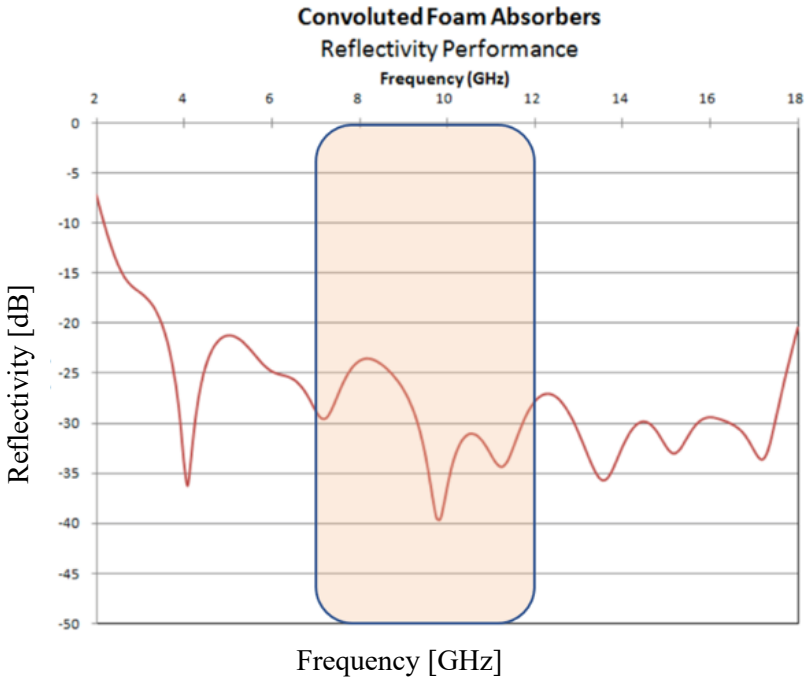

Figure 21: Reflectivity of MF32-0002-00 as a function of frequency.[18] The area of interest for our measurement is highlighted in the plot, going from 7 to 12 GHz.

[18] Source: MAST Technologies (www.masttechnologies.com).

5.4. Measurement Plan

The research program comprises four different types of measurements, data evaluation by the least-squares fitting. Measuring the microwave properties of the wire array as a function of the four geometrical variables required a different setup for each. As mentioned previously, the overall program is driven by our interest to find the most practical way to tune such an array *in situ* with a view to an actual haloscope experiment.

The term 'practical' here implies two things. First, it means being able to tune a single array over a large dynamic range in frequency (notionally a factor of 2), so one does not need to frequently interrupt a run to change out the array for another one covering a different frequency range. Second, a practical tuning scheme means one which possesses engineering simplicity but also sufficient precision by which the array can be tuned reproducibly in as small steps as required.

5.4.1 Square lattice arrays (b = a) as a function of the number of frames N

The research question here is what thickness of the wire array is required to see well-defined plasmonic behavior, i.e., a relatively sharp transition between t ~ 1 above the plasma frequency to t ~ 0 below. For this case of a square grid, a must equal b, which is 5.38 mm (same as the spacing between wires). Measurements were taken for N = 5, 10, 15 and 20. This data ultimately confirmed previous data taken with similar wire and plane spacing up to N = 20 [7]; we intended to extend these measurements to at least N = 25, but due to delivery problems with our usual machine shop, these measurements were not able to be carried out in time.

5.4.2 Transmission t as a function of grid geometry

Shifting two frame groups in the horizontal plane will result in a parallelogram constellation of wires in the x-y plane. Two specialized combination translation-rotation stages were designed and fabricated for measurements that deviated from rectangular unit cells, including wires in a parallelogram configuration. The concept of changing the symmetry of the array of parallel wires from rectangular to parallelogram by translating alternate interdigitated planes is shown in Fig. 22. While only a few specialized geometries have been explicitly calculated, not including this one for arbitrary displacements of interdigitated planes, the behavior generally expected is that the

plasma frequency will depend on the average density of the wires and should not depend critically on the specific lattice configuration. As experimentalists, however, we decided to perform this test anyway, even in the absence of a calculation.

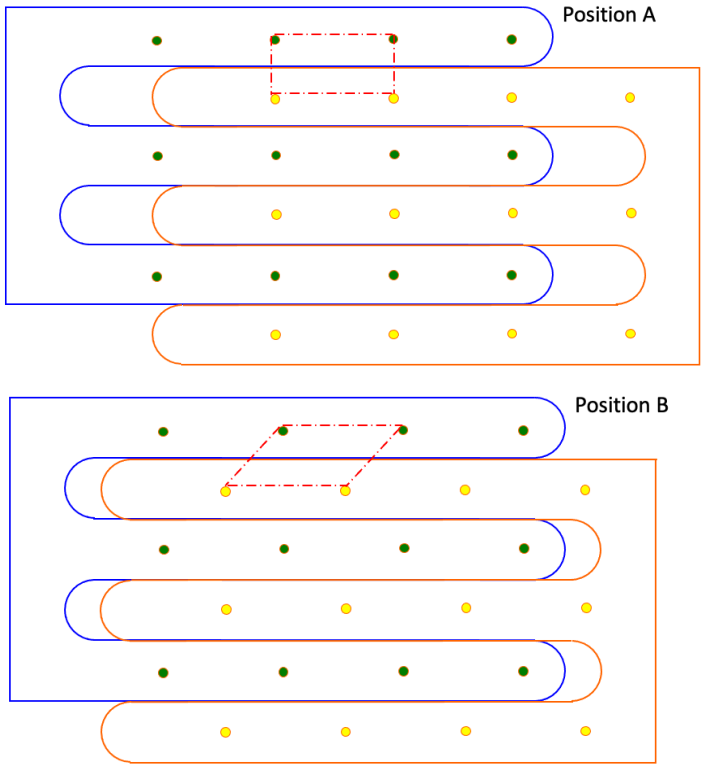

Figure 22: Relative translation of alternate interdigitated wire planes enables the symmetry of the array to be varied continuously (shown here in the x-z plane). Position A: Rectangular unit cell, Position B: Parallelogram unit cell.

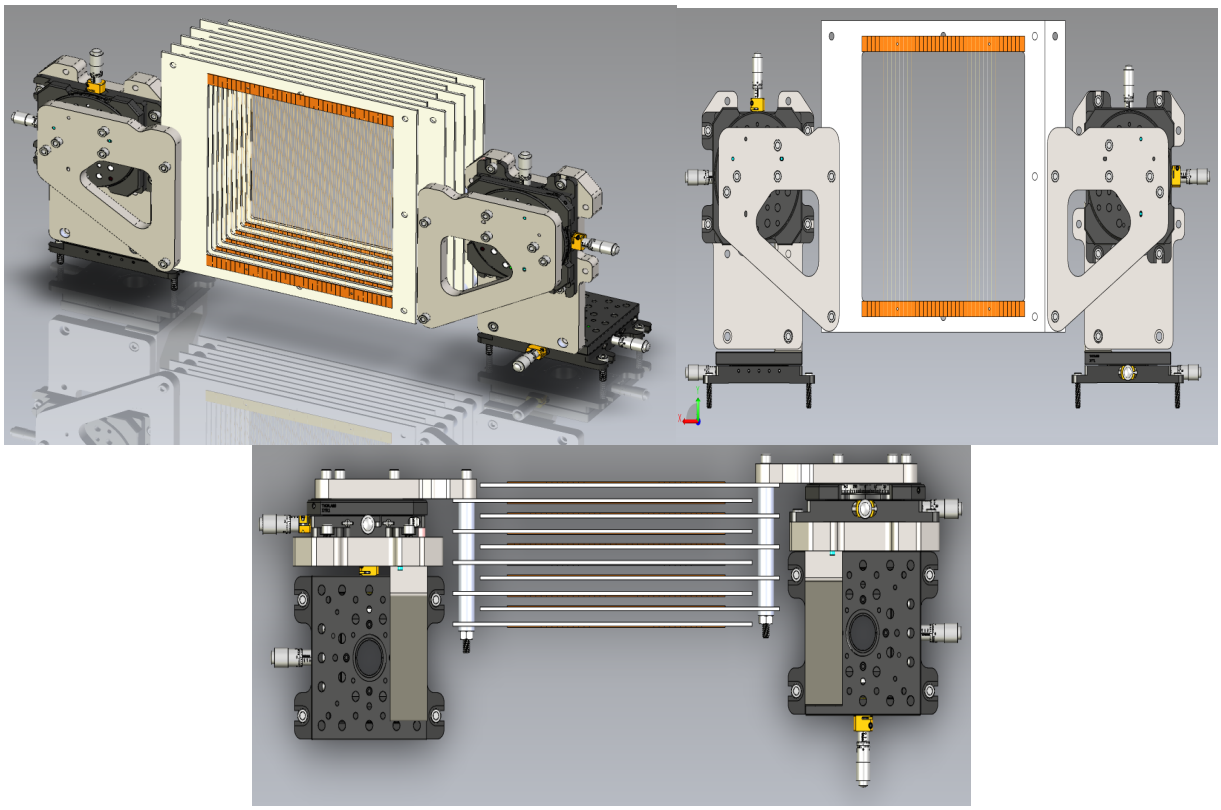

Figure 23: CAD modeling of the two precisions translation/rotation stages to manipulate translation in the x-axis and rotation in the x-y plane.

5.4.3 Transmission S_{21} as a function of frames spacing b

In this series of measurements, we vary the spacing of the full complement of planes (N = 20), defined as b, by changing the number of thin nylon spacers which separate the steel frames. These spacers are 0.6 mm in thickness and are cut into washers so they may conveniently fit over the four nylon threaded rods. In this manner, we can break the square symmetry and determine the plasma frequency and loss term for configurations of both a < b and a > b. In this case, however, we have a theory that has been worked out numerically with which we can compare [6].

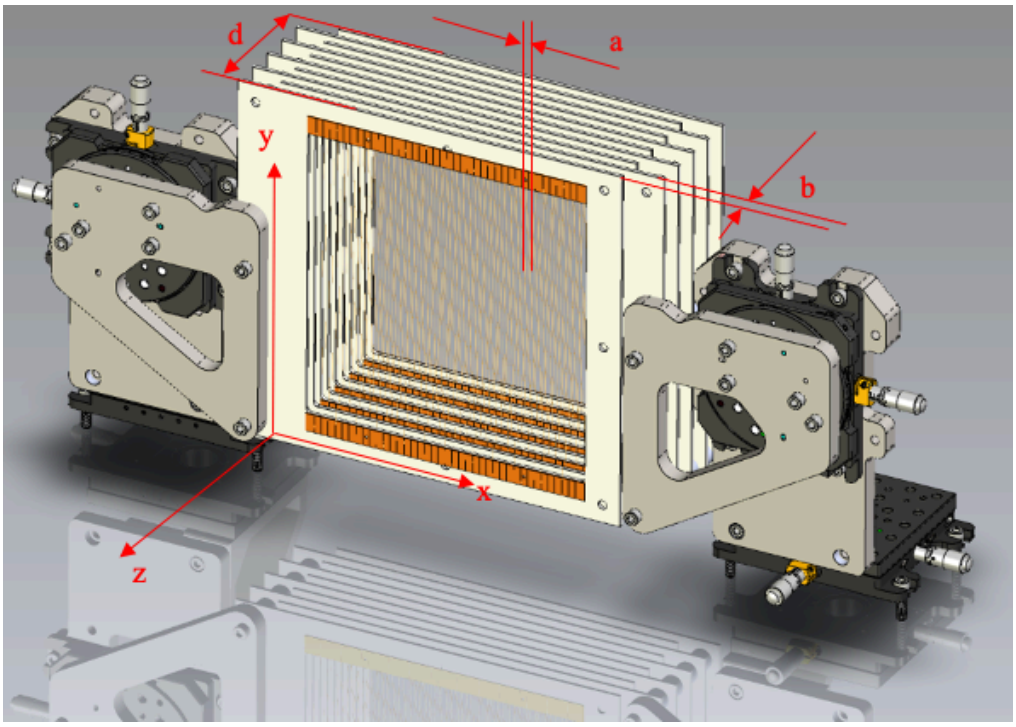

Figure 24: CAD modeling of shift experiment with schematics to define parameters wire spacing a, frames spacing b, and total frames assembly thickness d in the coordinate system of frames assembly.

5.4.4 Transmission S_{21} as a function of θ

In this series of measurements, we examine the transmission as a function of the angle of the wire arrays θ with respect to the polarization axis z of the microwave beam. For this purpose, we assembled the full complement of 20 frames alternating in +θ and –θ tilt around the z-axis, which is the propagation direction.

5.5 Theory of Transmission Through a Medium with Complex Permittivity

We characterize our wire array metamaterials primarily by measurements of the frequency-dependent microwave transmission through the array. To connect the measurements with the physics parameters we are interested in, ω_p, Γ and d, it is first useful to exhibit the solution of Maxwell's equations for wave propagation through a slab with complex dielectric constant or permittivity. We follow the treatment of Yahalom et al. [34], who define the frequency-dependent relative permittivity as

$$\epsilon_r(f) = \epsilon'(f) - j \cdot \epsilon''(f)$$

where $\epsilon'(f)$ and $\epsilon''(f)$ are the real and imaginary components of the dielectric constant [34].

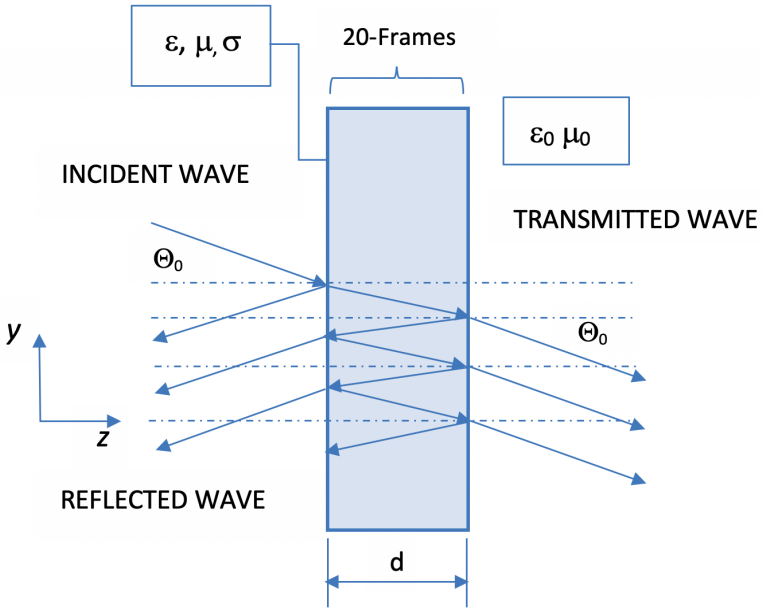

Figure 25: Wave propagation through a dielectric slab.

Following Lawson et al. [2], who proposed the tunable plasmonic haloscope, we model the metamaterial as having a complex permittivity $\epsilon_r(f)$ described by a simplified Drude model [4]:

$$\epsilon_r = 1 - \frac{\omega_p^2}{\omega^2\left(1 - j\frac{\Gamma}{\omega}\right)}$$

by which one can immediately identify $\epsilon' = Re(\epsilon_r)$ and $\epsilon'' = Im(\epsilon_r)$ as

$$\epsilon' = \left(1 - \frac{\omega_p^2}{\omega^2 + \Gamma^2}\right)$$

and

$$\epsilon'' = \left(\frac{\Gamma}{\omega}\right)\frac{\omega_p^2}{\omega^2 + \Gamma^2}$$

where Γ represents the loss term, which has units of Hz.

For a lossless plasma, the cutoff frequency equals the plasma frequency. For a lossy plasma, there is an exponentially damped propagating wave down to a cutoff frequency $\omega_{cutoff} = (\omega^2 + \Gamma^2)^{\frac{1}{2}} < \omega_p$. For an electromagnetic wave incident on a finite slab of plasma, one will have a transmitted wave for arbitrarily low frequencies, of course, even though only exponentially decaying waves are supported by the plasma.

The amplitude of the transmitted wave can be expressed relative to the amplitude of the incident wave in full generality as

$$E_{out}(f) = E_{in}(f) \cdot e^{-[\alpha(f) + j\beta(f)]\cdot d}$$

where d is the width of the dielectric material, here being the wire array metamaterial. As given in Yahalom [34], α(f) and β(f) can be expressed as

$$\alpha(f) = \frac{2\pi f}{c}\sqrt{\frac{\varepsilon'(f)}{2}\left\{\sqrt{1 + tg^2[\delta(f)]} - 1\right\}}$$

$$\beta(f) = \frac{2\pi f}{c}\sqrt{\frac{\varepsilon'(f)}{2}\left\{\sqrt{1 + tg^2[\delta(f)]} + 1\right\}}$$

where the loss tangent is given by

$$tg[\delta(f)] = \frac{\epsilon''(f)}{\epsilon'(f)}$$

For the electric field vector lying in the plane of incidence (TM-wave) or perpendicular to it (TE-wave), the field reflection coefficient is given by

$$\rho_{0-TM} = \frac{\sqrt{\varepsilon_r - \sin^2(\theta_0)} - \varepsilon_r \cos(\theta_0)}{\sqrt{\varepsilon_r - \sin^2(\theta_0)} + \varepsilon_r \cos(\theta_0)} \quad , \quad \rho_{0-TE} = \frac{\cos(\theta_0) - \sqrt{\varepsilon_r - \sin^2(\theta_0)}}{\cos(\theta_0) + \sqrt{\varepsilon_r - \sin^2(\theta_0)}}$$

All our measurements were carried out for normal incidence of the beam ($\theta = 0$), for which the two expressions above are identical. The field transmission coefficient [34] is thus given by

$$t = \frac{\left(1-\rho_0^2\right)e^{-jk_z(f)d}}{1-\rho_0^2 e^{-j2k_z(f)d}} = \frac{\left(1-\rho_0^2\right)e^{-(\alpha+j\beta)\cos(\theta)d}}{1-\rho_0^2 e^{-2(\alpha+j\beta)\cos(\theta)d}}$$

Note that t is an expression for the ratio of the transmitted to the incident electric field, or equivalently S_{21}; it is a complex number represented by amplitude and phase, both of which are recorded by the Vector Network Analyzer. As the magnitude of S_{21} is read out of the VNA in decibels [dB], we perform the fits to the scalar logarithmic gain, defined as $g = 20 \log_{10}(|S_{21}|)$ [dB], which returns the key parameters ω_p, d, and Γ.

5.6 Experimental Results

5.6.1 Data Reliability

To correctly interpret our data, it is essential to ensure that they are reproducible over the time frame during which they are taken (typically minutes) and within the time frame of other measurements with which they may be compared (hours to months). We determine the frequency-dependent scalar logarithmic gain by means of a four-run cadence alternating measurements with the wire array (i) out, (ii) in, (iii) out, (iv) in. Each measurement takes less than two minutes of time. Care is taken not to disturb the setup while the array is moved in or out of position, i.e., the Eccosorb baffles, the two microwave horns, the cables, and the VNA are not moved or bumped. The stability of the results within the cadence is depicted in Fig. 26.

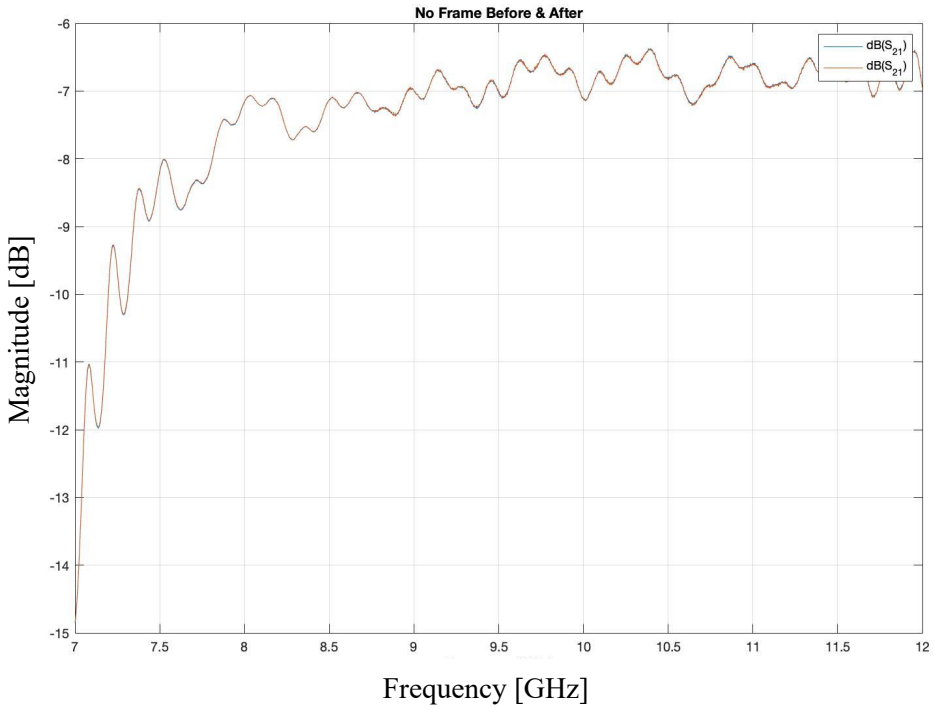

Figure 26: Comparison of the two array-out measurements within one four-run cadence. Note that the two curves overlap one another perfectly.

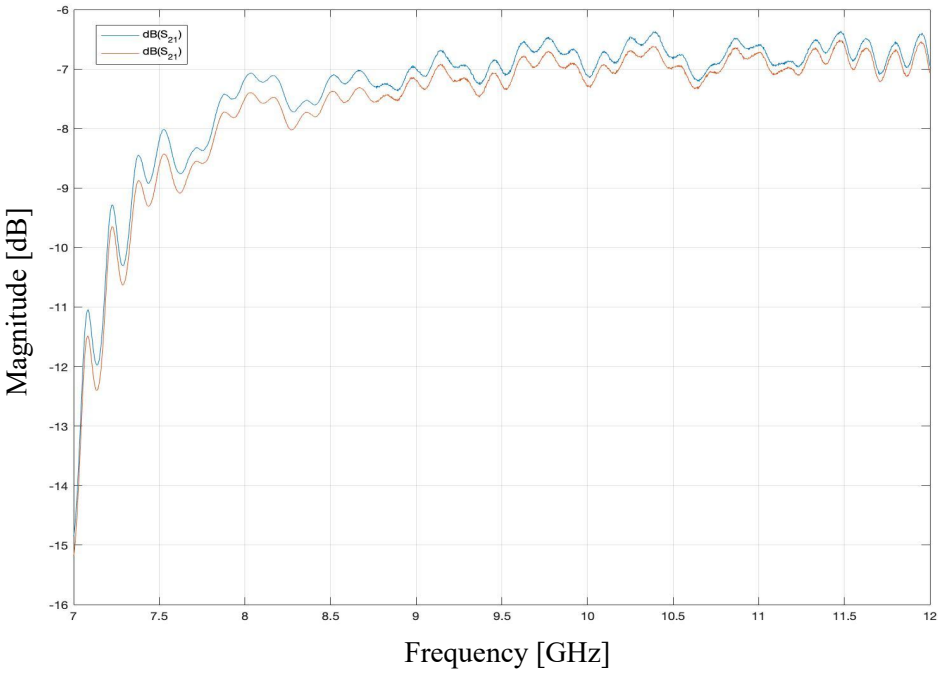

Figure 27: Array-out runs separated by a month (July-August 2020); the difference is a constant offset of less than 0.25 dB.

Data taken separated by a month was perfectly reproducible in shape but with a constant offset of typically less than 0.25 dB, as seen in Fig. 27.

5.6.2 S2P Data File Format

The data from VNA are stored as S2P files, which include S_{11}, S_{21}, S_{12}, and S_{22}. Table 2 shows an example of the actual data columns.

Column #1	#2	#3	#4	#5
ω	S_{11}		S_{21}	
Hz	dB	Phase	dB	Phase
7000000000	-8.94E+00	1.23E+02	-6.46E+01	-1.03E+02
7001667222	-9.25E+00	1.26E+02	-6.39E+01	-1.09E+02
7003334445	-9.48E+00	1.30E+02	-6.37E+01	-1.12E+02
7005001667	-9.62E+00	1.34E+02	-6.34E+01	-1.19E+02
7006668890	-9.66E+00	1.38E+02	-6.36E+01	-1.24E+02
7008336112	-9.59E+00	1.42E+02	-6.38E+01	-1.25E+02

Column #1	#6	#7	#8	#9
ω	S_{12}		S_{22}	
Hz	dB	Phase	dB	Phase
7000000000	-6.54E+01	-1.09E+02	-2.24E+00	-9.39E+01
7001667222	-6.51E+01	-1.13E+02	-2.28E+00	-9.47E+01
7003334445	-6.35E+01	-1.15E+02	-2.31E+00	-9.55E+01
7005001667	-6.35E+01	-1.20E+02	-2.37E+00	-9.63E+01
7006668890	-6.49E+01	-1.26E+02	-2.41E+00	-9.71E+01
7008336112	-6.35E+01	-1.34E+02	-2.45E+00	-9.80E+01

Table 2: Data format of S2P files for the transmission S_{21} measurements. In this example, the first six rows of R4, 20 frames transmission of a square grid wire constellation is presented.

5.7 Tests and Measurements of Wire Array Assembly

A total of four experiments were carried out to determine the behavior of the wire arrays combined of 20 metallic frames tested inside a microwave-quiet environment. We measure the transmission S_{21} [dB][19] as a function of the number of frames, the effect of grid geometry, the frame spacing, and the wire array rotation in the polarization plane. The parameters of interest are ω_p [GHz], Γ [GHz], and d [cm].

5.7.1 Transmission as a Function of Number of Frames

The first set of measurements taken were with a square lattice, a = b = 5.38 mm, and the first question addressed was for what depth of metamaterial, i.e., number of planes, does one recognizably attain full plasmonic behavior? Results of the transmission coefficient as a function of frequency for N = 5, 10, 15, and 20 frames are displayed in Fig. 28-a. As the number of planes is increased, the curve steepens to a cutoff around 11 GHz. With the array removed, the field transmission, t = 1, was determined to be at -6.53 dB, which is the average loss for a frequency interval from 7 GHz to 12 GHz.

[19] The S_{21} data are computed as $g[dB]=20*Log_{10}(|S_{21}|)$.

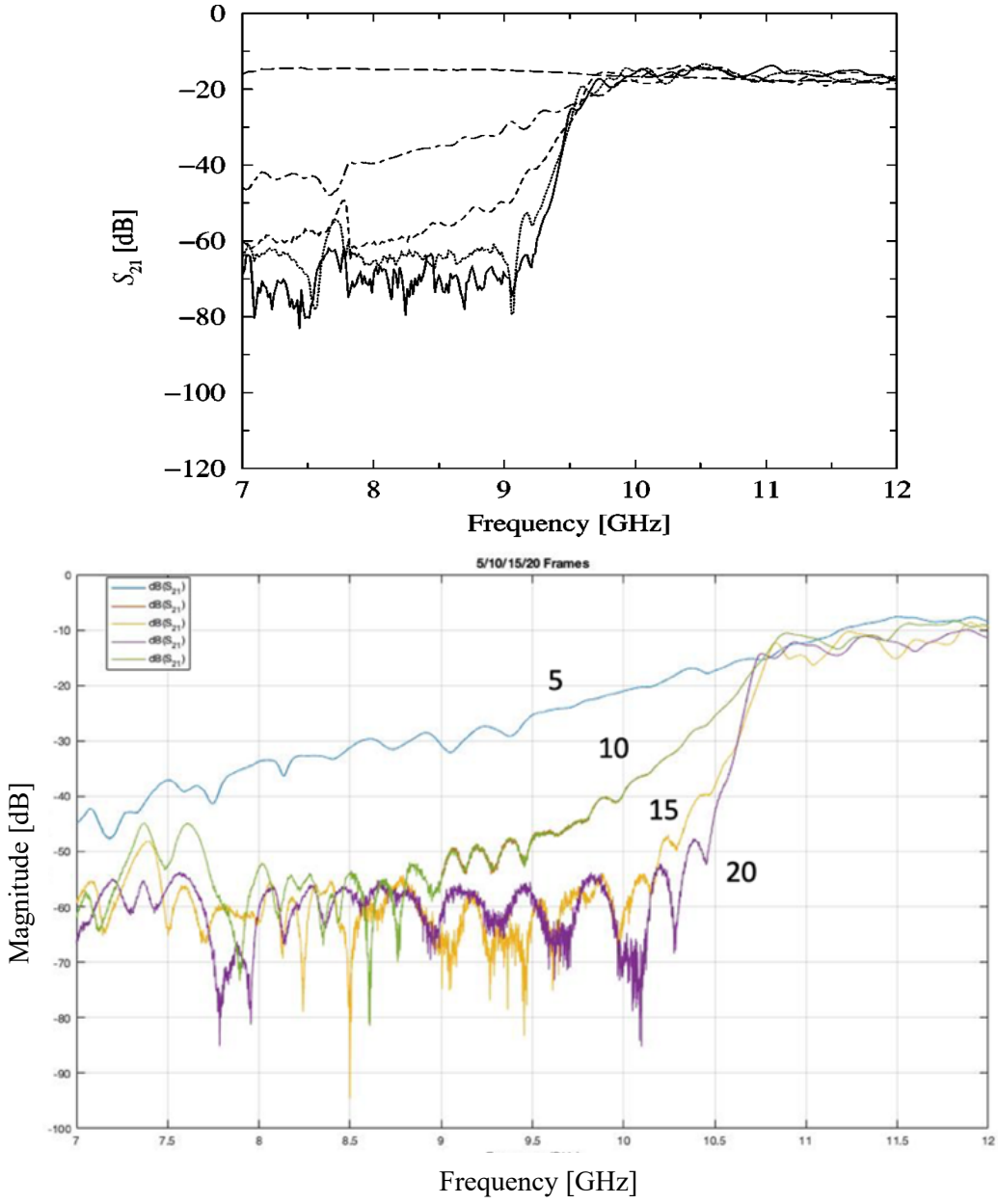

Figure 28: The scalar logarithmic gain as a function of frequency for a various number of planes N = 5, 10, 15, and 20, with a wire radius of 25 μm and spacing of 5.38 mm, in a square array. The same data for N = 5, 10, 15 and 20 planes with similar parameters, from a previous study, with r = 30 μm, a = 6 mm in a square array [7]. A minor difference between this measurement and ours is that their wires were mounted on a foam substrate (Rohacell HF 51, ϵ = 1.07) for ease of construction, whereas in our measurements, the wires were strung in free space.

The data are in excellent qualitative agreement with previous results of Gay-Balmaz et al. [7], who likewise saw the evolution of bulk plasmonic behavior by increasing the number of wire planes (Fig. 28-b); in their case, the wire radius was r = 30 μm and the square lattice wire spacing, a = 6 mm.

Fig. 29 shows the S_{21} for one case of 20 planes to highlight a few features of the data. Well below the falloff, there is a noise floor around – 60 dB which represents a flat background of irreducible noise. In the least-squares fitting described below, the noise floor can either be included as one of the constants to be determined, or the noise floor can be eliminated entirely from the fit (i.e., exclude all data below around 10.5 GHz here). Both have been tried, and the results did not significantly depend on the procedure.

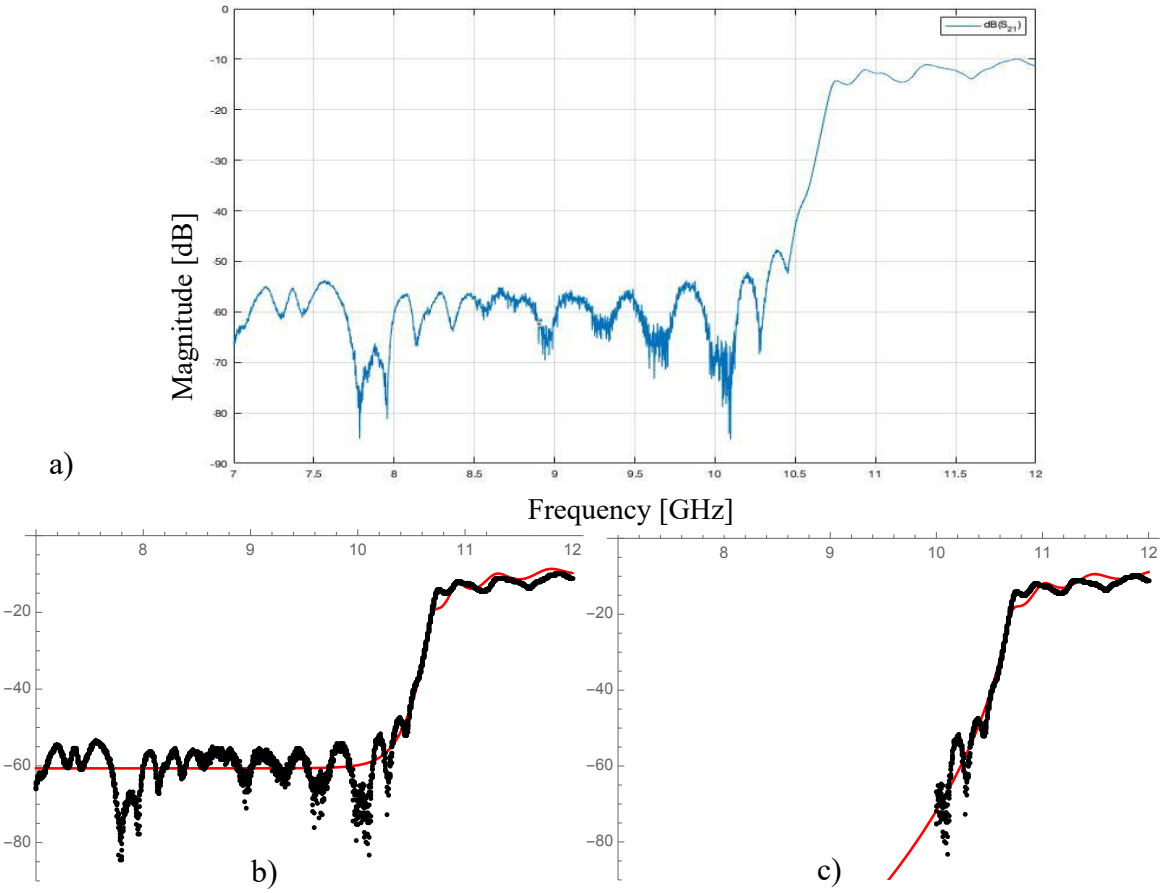

Figure 29: *a) Experimentally measured S_{21} for the case of a square lattice and 20 frames. b) The same data and least-squares fit (red) where the noise floor has been included in the data and a control parameter in the fit. c) The data and fit (in red), but where the data have been truncated to eliminate the noise floor, as well as the control parameter in the fit.*

Above the sharp break in the curve, where $g \sim 1$, one sees oscillatory behavior, which is not an artifact, but which is generally well reproduced in the fits. The values of the three parameters obtained through least-squares fits to our data for each N are presented in Table 3.

Measured	Number of Frames	d [cm] Measured	d [cm] Experiment	ω_p [GHz] Theory	ω_p [GHz] Experiment	Loss Γ Experiment
R1	5	2.3	2.75	10.80	10.50	0.4102060
R2	10	4.9	5.47	10.80	10.518	0.0266216
R3	15	7.5	8.25	10.80	10.526	0.0349151
R4	20	10.2	11.28	10.80	10.437	0.0424495

Table 3: Results from measurements of transmission power as a function of N, at a plasma frequency of 10.8 GHz, and a = b =5.38 mm.

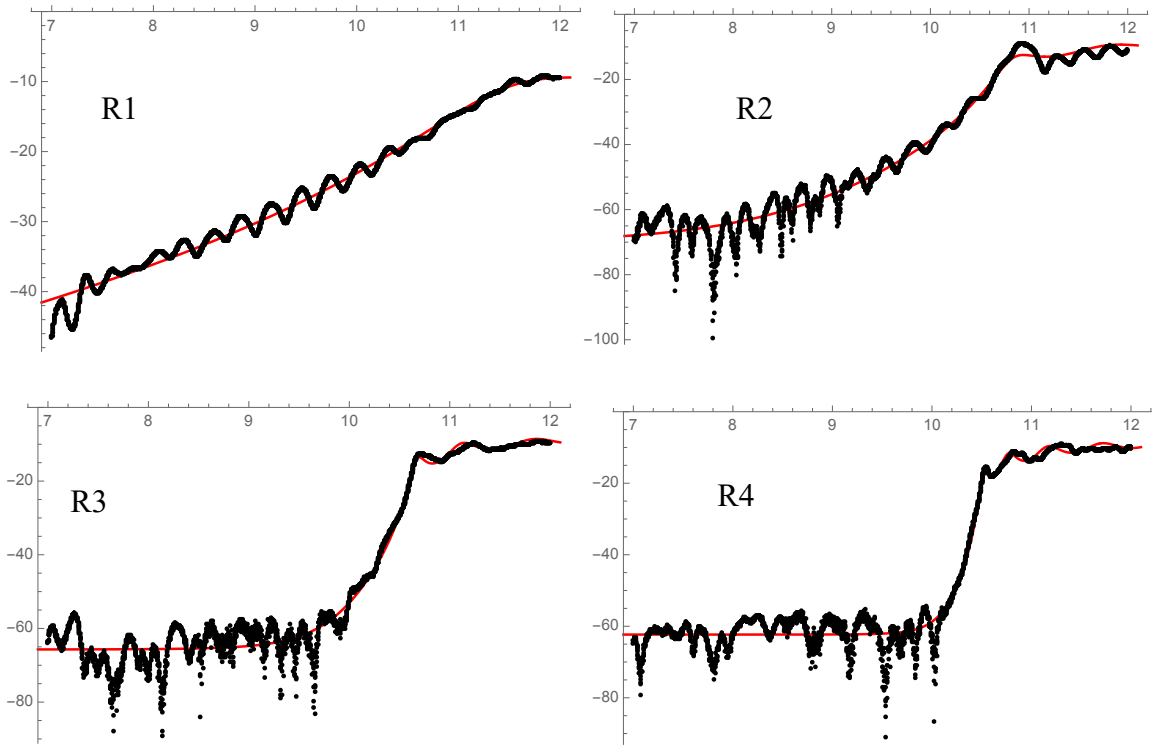

Figure 30: Results of S_{21} measurements for 5, 10, 15, and 20 frames with fitted curves marked in red. R1: fitted curve of measured S_{21} for 5 frames, R2: fitted curve of measured S_{21} for 10 frames, R3: fitted curve of measured S_{21} for 15 frames, R4: fitted curve of measured S_{21} for 20 frames.

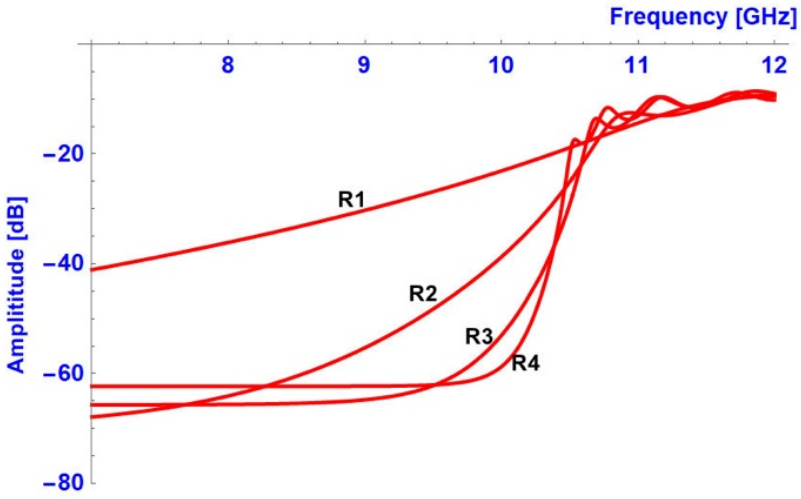

Figure 31: *The fitted curves for the increased number of frames with R1=5, R2=10, R3=15, and R4=20 frames.*

The plots in Fig. 31 are generated by fitting the data with the formula for the transmitted power t after traversing a slab described by a complex dielectric constant [34]. A simple Drude model [3] is invoked for the metamaterial slab, which prescribes the functional form for the real and imaginary parts of the dielectric constant, and from which the fit returns the plasma frequency ω_p, the thickness d, and the loss term Γ.

The comparison is clearly showing that with an increased number of frames, metamaterial behavior becomes more evident, and the curve becomes sharper as we increase the number of frames (Fig. 30).

5.7.2 Effect of Grid Geometry on Transmission

So far, I have experimented with rectangular and square order of grid as seen in the x-z plane perspective. We want to examine if the configuration of the wires in the lattice has any effect on amplitude or frequency. For this purpose, I designed a Phase II experiment setup. A schematic of the experiment setup is shown in Fig. 32.

The frames are subsequently attached to x-y and x-z positioning stages. I selected a frame spacing of 9 mm, with a fixed wire spacing of a=5.38 mm. As I shift the second group of frames by actuating the micrometer, I can now manipulate the constellation of the grid in the x-z plane as presented in Fig. 33. This allows us to continuously shift the interdigitated planes from a rectangular lattice to where the unit cell is a parallelogram. The result was as expected, there was no change in the frequency of 8.9 GHz as the average density of wires remains the same, and thus the plasma frequency remains the same, as indicated in the equation:

$$\omega_p^2 = \frac{ne^2}{\varepsilon_0 m_{\text{eff}}}$$

The number density of electrons n is constant, and it is not dependent on the grid geometry. Fig. 34 shows the frequency plot at which the experiment was executed.

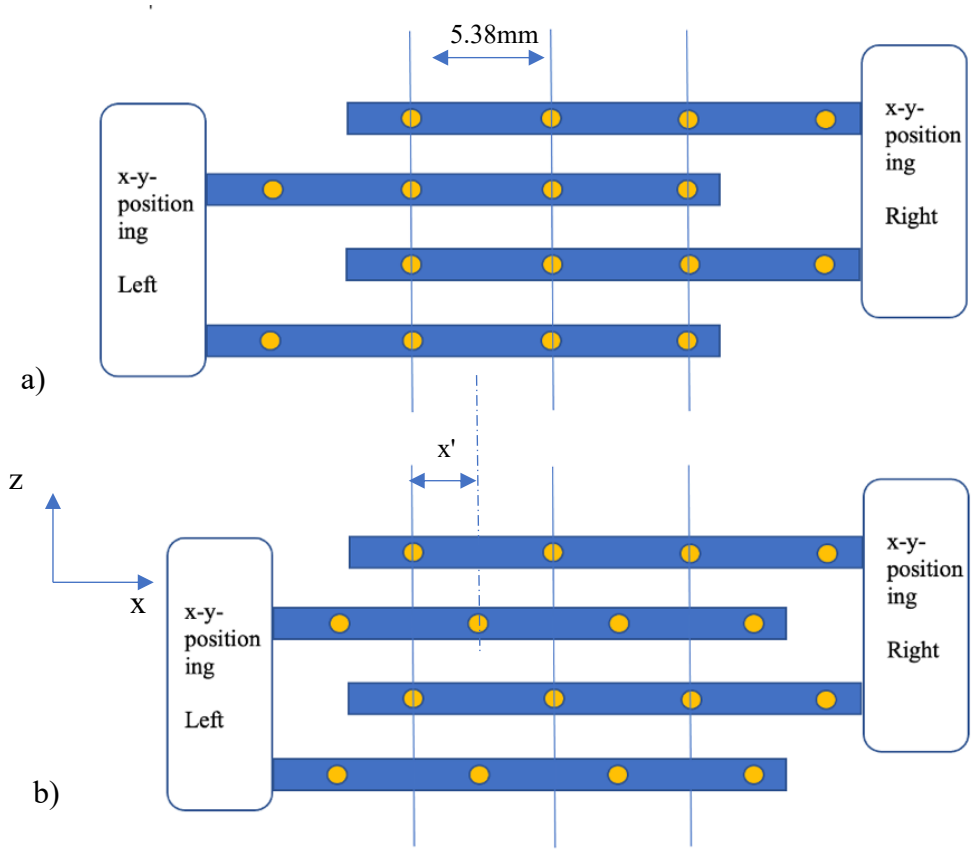

Figure 32: The two limiting cases of the wire array lattice in the x-z plane for interdigitated planes. a) Rectangular lattice. b) For any other shift x' ≠ a, the unit cell is a parallelogram.

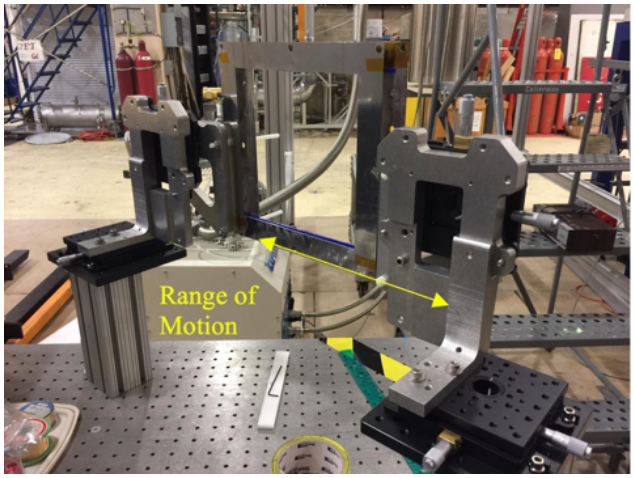

Figure 33: Experiment setup for shift and tilt measurements.

a)

b)

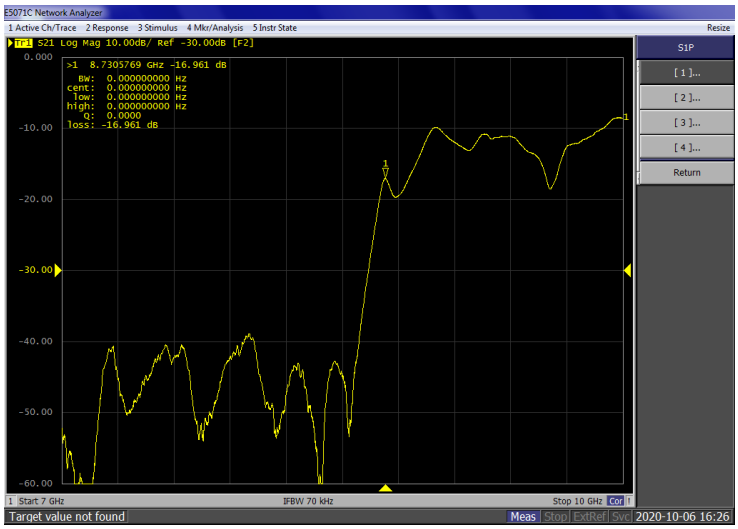

Figure 34: Phase II experiment with 16-frames. This plot is generated by measuring transmission for wire grid assembly in a parallelogram grid. As we actuate the micrometer to change the position of wires in space from a) rectangular to b) parallelogram lattice, the frequency does not change.

5.7.3 Dependence on the Wire Array Spacing

Two parameters control S_{21}, namely the spacing between wires, a, and spacing between frames, b. I measured S_{21} by varying the space between frames, and with it, the ratio of a/b as the spacing between wires is fixed. I ran tests for various values of b. Fig. 35 shows the dependence on how far apart the frames are, which is included in Belov equation[20] [6]. With a frame thickness of 1.7 mm, and each spacer thickness measures 0.6 mm, we measured and computed t. Results from experimental values and predictions are shown in Table 4.

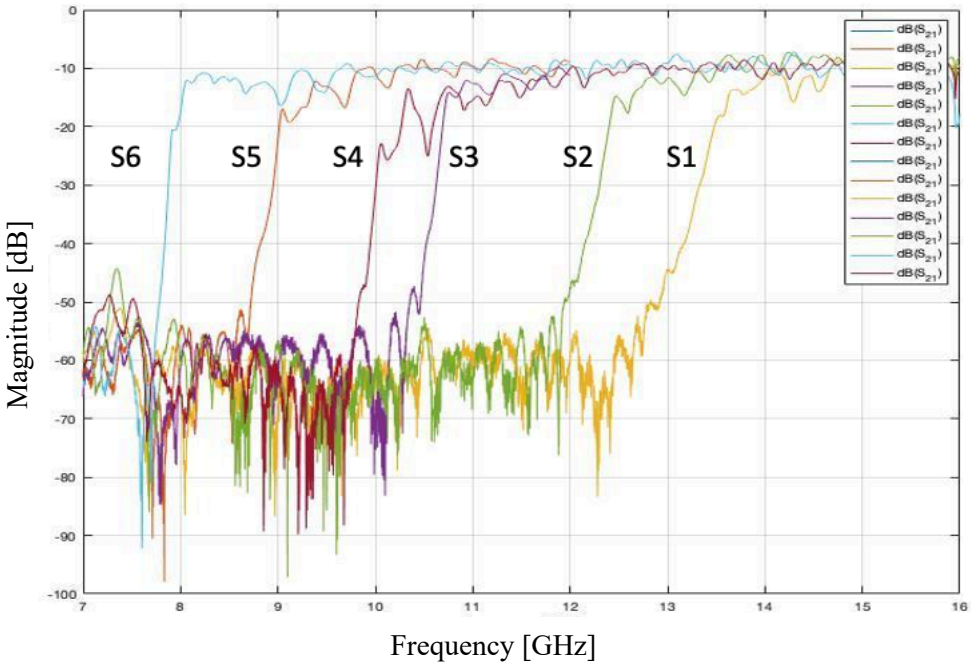

Figure 35: Plots for various values for wire array spacing b. It shows that with decreasing values for b, we gain higher frequencies.

[20] Equation (10) [6].

Cases	b [mm]	#Spacer	d [cm] Measured	d [cm] Experiment	ω_p [GHz] Theory	ω_p [GHz] Experiment	Loss Γ Experiment
S1	3.58	3	7	7.5	13.78	13.3	1.59787
S2	4.18	4	8	8.7	12.68	12.3	0.0458897
S3	5.38	6	10	11.6	11.0	10.6	0.114631
S4	5.98	7	11.5	11.8	10.39	9.9	0.261109
S5	7.18	9	14	10.9	9.35	8.95	0.164386
S6	8.98	12	17	19.3	8.19	7.8	0.0207532

Table 4: Experimental data and predictions from Belov equation[21] [6] on the plasma frequency as a function of the wire array plane spacing b, where the wire spacing has been fixed at a=5.38 mm.

As we see in the results of the experiment, it is clear that as we increase the number of frames, the curve of t becomes steeper at ω_p , and at 20 frames, a step-function-like can be seen at the cutoff frequency. This was expected since we are increasing the number density of plasmon by adding more layers of metallic surfaces. The experiment results (shown in red) are in good match with the computed values of the analytical solution, as seen in Fig. 36.

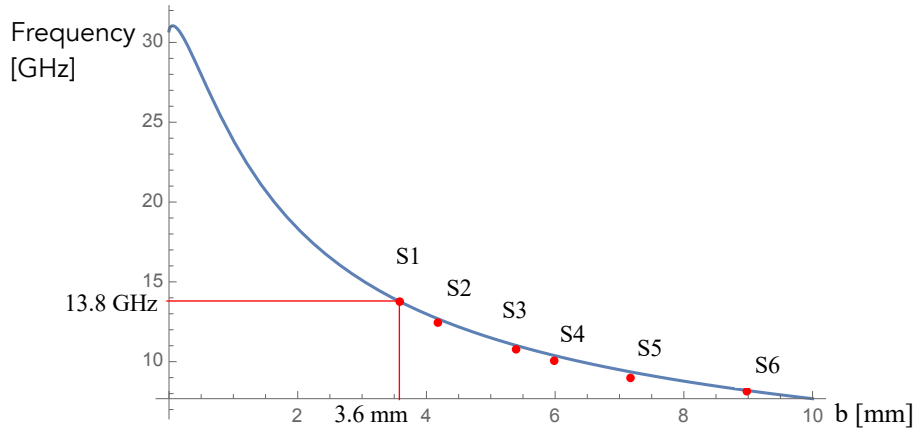

Figure 36: Computed Belov equation[22] [6] plot vs. experimental data marked red (true) displays frequency as a function of planes spacing b. The measured data fits perfectly on the computed curve.

[21] Equation (10) [6].
[22] Equation (10) [6].

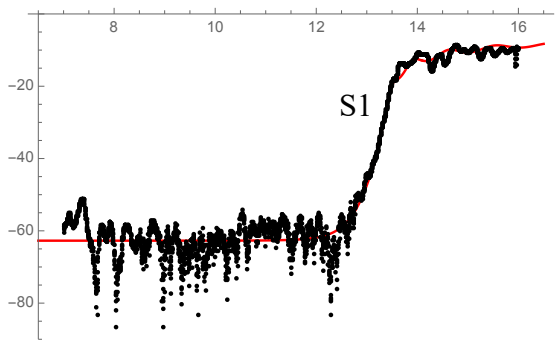

S1: TEST OF 20-FRAMES WITH b1=3.58 mm

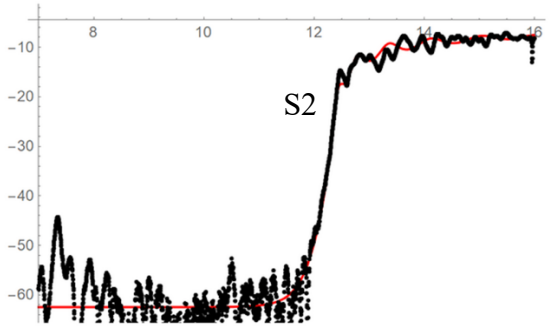

S2: TEST OF 20-FRAMES WITH b2=4.18 mm

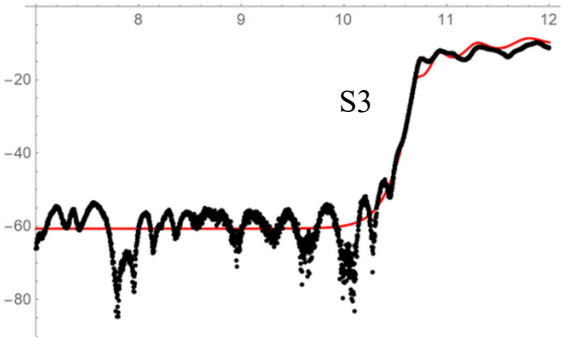

S3: TEST OF 20-FRAMES WITH b3=5.38 mm

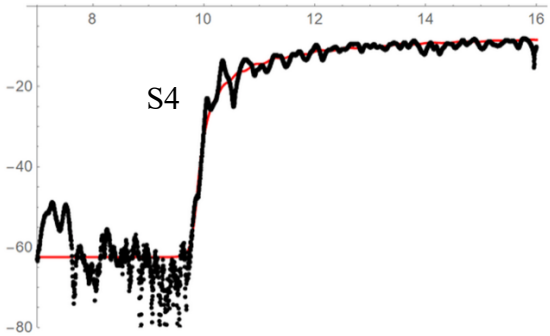

S4: TEST OF 20-FRAMES WITH b4=5.98 mm

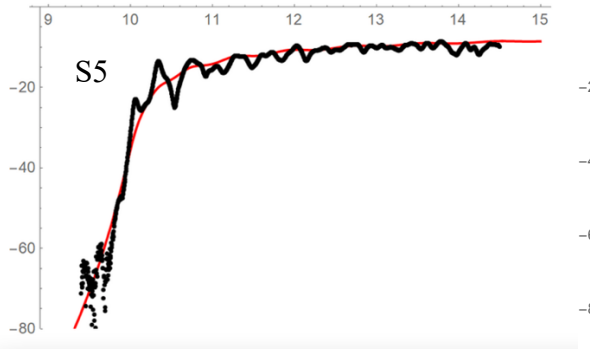

S5: TEST OF 20-FRAMES WITH b5=7.18 mm

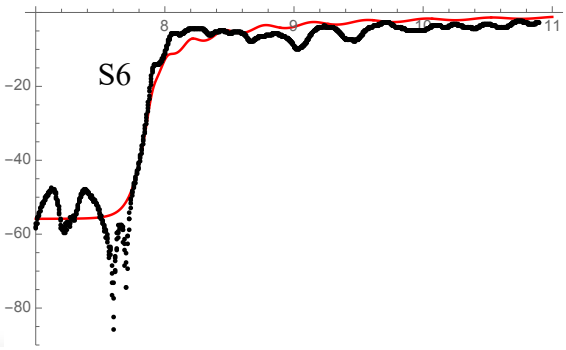

S6: TEST OF 20-FRAMES WITH b6=8.98 mm

Figure 37: Data fitting applied to S1 to S6 with frame spacing b as a variable (shown in red).

Fig. 37 shows the effect of variable wire array spacing b. The results of fittings are combined in Fig. 38.

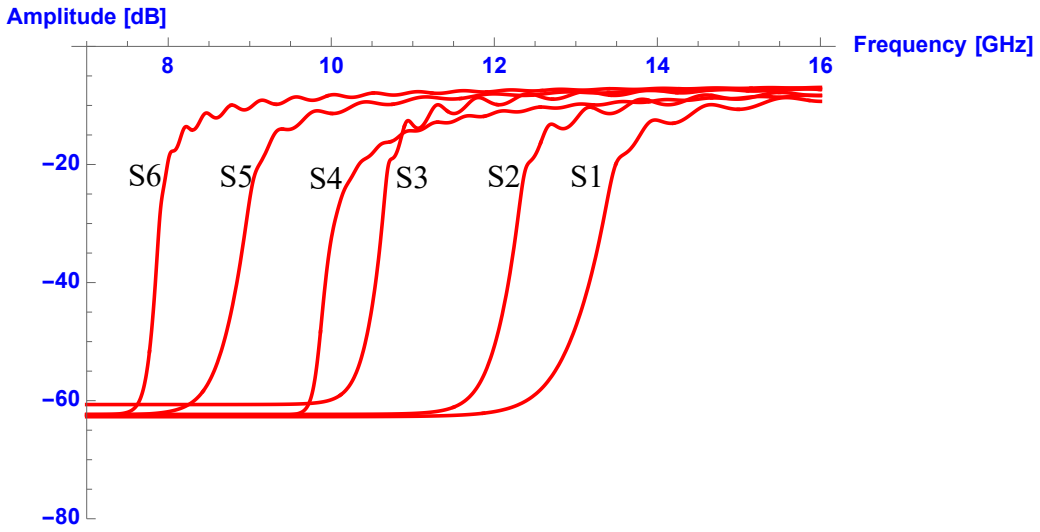

Figure 38: Combined fitting plots of change in frequency as the frame's spacing b increases, with b1=3.58 mm, b2=4.18 mm, b3=5.38 mm, b4=5.98, b5=7.18 mm, and b6=8.98 mm.

The experimental measurement results of plasma frequency ω_p, wire array plane spacing b, and wire array assembly thickness d are in good agreement with the computed results (Table 4). The frequency shifts to higher values as the space between frames become smaller.

5.7.4 Dependence on Angular Manipulation

To improve the design of the experiment, we added six panels of Eccosorb, a highly absorbing foam of microwaves; we call it the Dark Cube, where all measurements took place inside the cube. The assembled frames can now be placed inside the Dark Cube. Originally, the interdigitated frames were mounted on the two micrometer stages with 3-Degrees of Freedom, but this arrangement suffered from a small areal overlap, with the result that there was some occlusion of the microwave beam by the frames, making the data noisier. In our second attempt, we directly stacked the frames on top of one another at alternating angles of ±Θ, which had a much larger open area, and thus no occlusion of the beam. This gave us much cleaner results.

To examine the effect of angular tilt in the x-y polarization plane, we stack the frames in alternating positions as + Θ for the first frame followed by - Θ position for the next frame. This constellation will allow us to match the size of the horns with the overlapping area. Fig. 39 shows an example for various Θ positions.

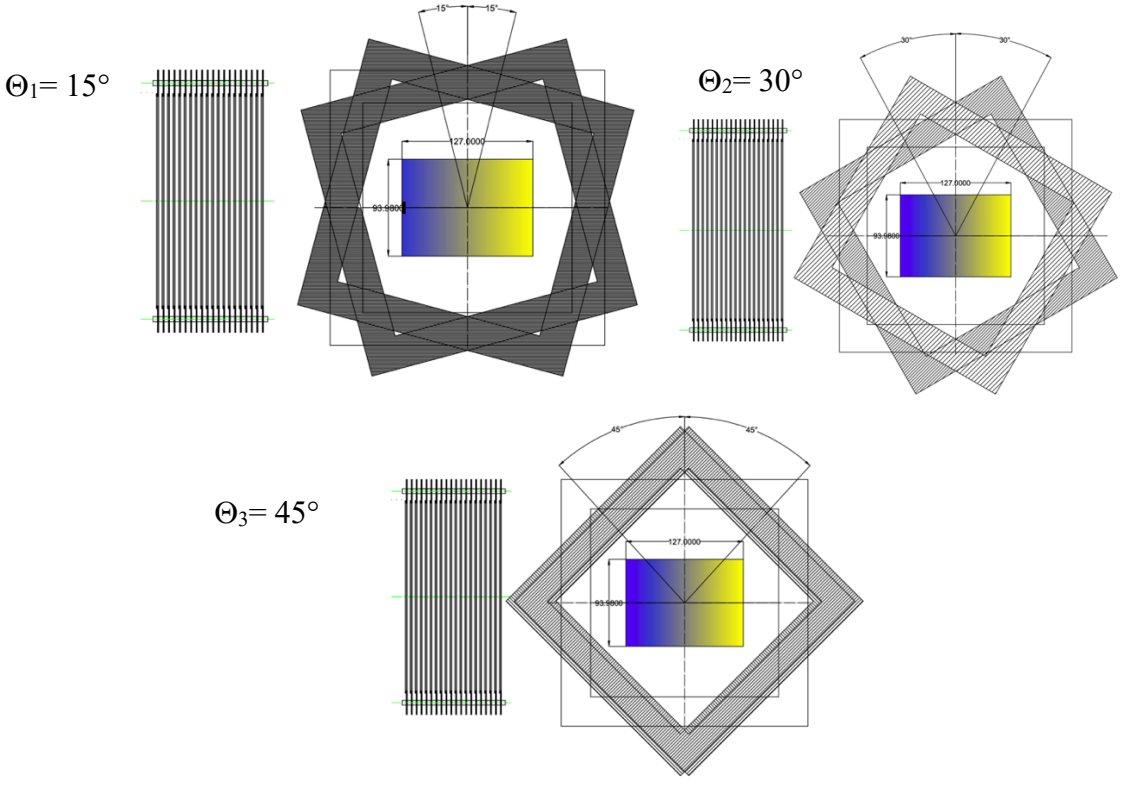

Figure 39: Schematics of frame positioning normal to the optical axis at various angles Θ.

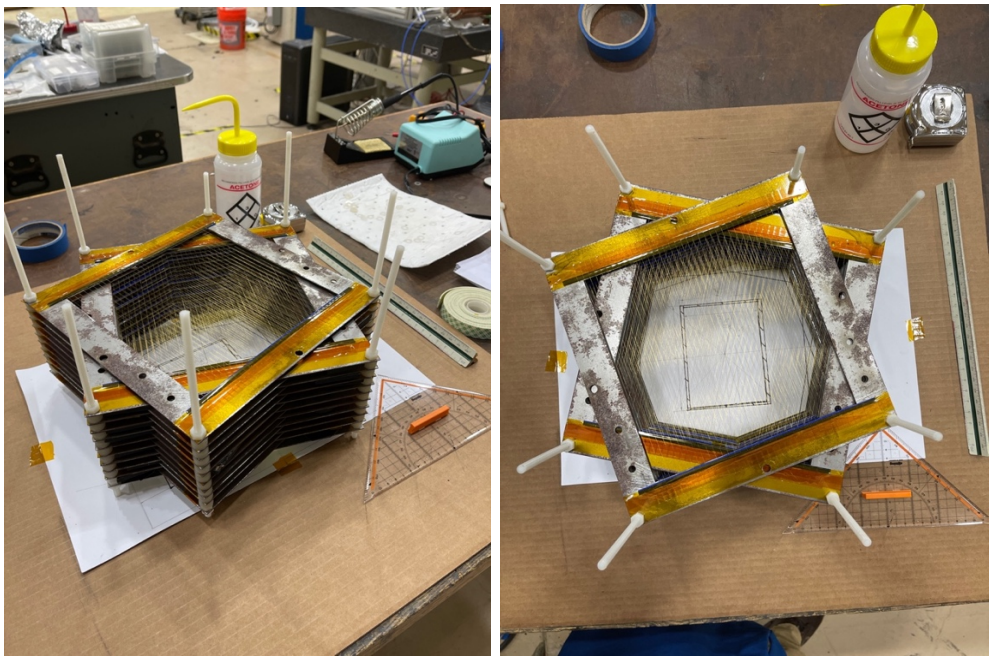

Figure 40: 20-frames assembly with alternating planes oriented by ±15 degrees, perpendicular to the optical axis, with the 1:1 scale drawing of the horn antenna aperture shown in the background.

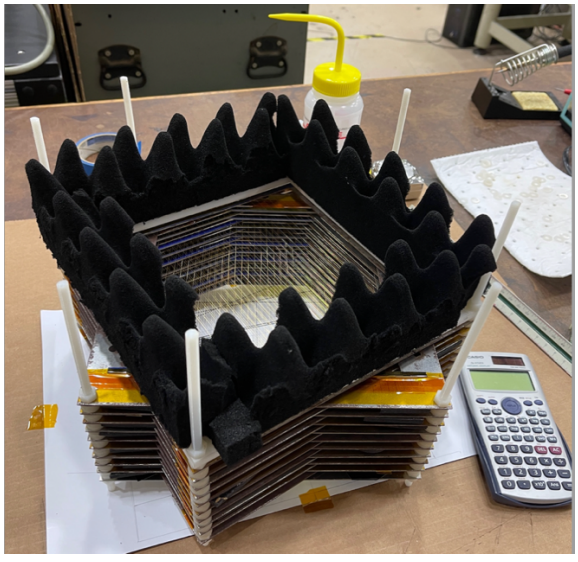

Figure 41: Frames assembly shown with Eccosorb layers to prevent back reflection of EM-waves. Nearly all metallic surfaces are covered with Eccosorb, including the support structures.

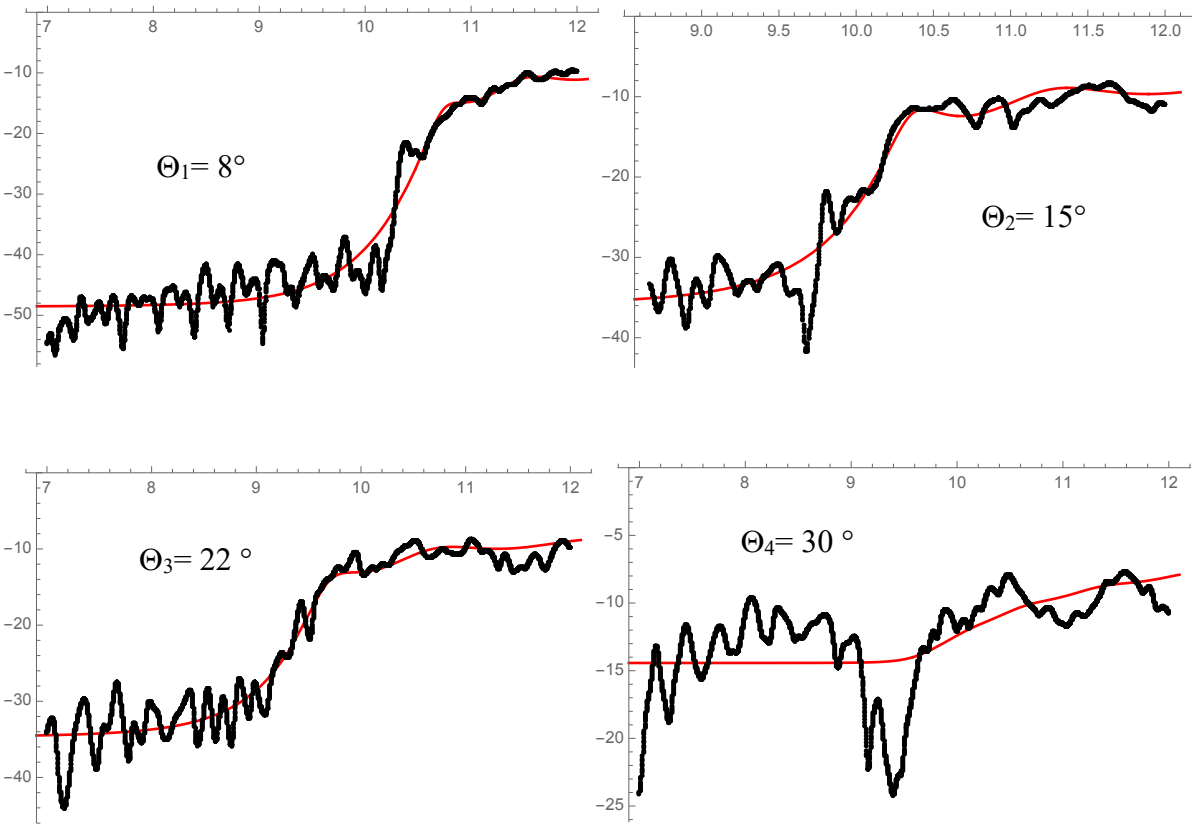

Figure 42: Transmission coefficient as a function of angular tilt in x-y-plane of 20 frames with fitting shown in red.

The results from the later setup are satisfactory. Compiling the data in Matlab, we see a clear rise of the noise floor at frequencies lower than the cutoff frequency. The high pass filter nature of the metamaterial clearly degrades for even small angular shifts; thus, we did not examine any angles beyond 30 degrees. Fig. 43 shows the combined fitted data.

Displaying all fitting plots in a single plot, we can see clearly that the frequency decreases with increased Θ, and the noise floor increases dramatically toward t=1. As for frames total width d, physically, it is constant at 10 cm, but when applying fitting to the data, it will give us variable values. One interesting observation, that when we assume that d is a constant, the code still gives us the same frequency regardless of d values.

Angle	d [cm] Measured	d [cm] Experiment	ω_p [GHz] Theory[23]	ω_p [GHz] Experiment	Losses Γ Experiment
Θ0= 0°	10	10	10.29	10.29	0.114631
Θ1= 8 °	10	6.21	n/a	10.47	0.226203
Θ2= 15 °	10	5.73	n/a	10.05	0.142266
Θ3= 22 °	10	5.64	n/a	9.35	0.278597
Θ4= 30 °	10	9.8	n/a	9.59	0.569054

Table 5: Computed values for frames assembly of thickness d and frequency as produced by the experiment for angles 8°, 15°, 22°, and 30°, respectively.

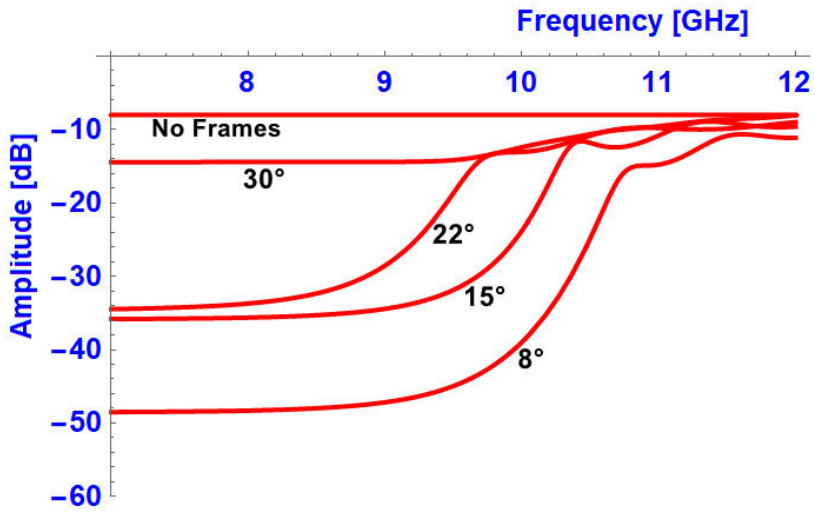

Figure 43: Plot of least-squares fits for angles 8°, 15°, 22°, and 30°.

[23] No theory for plasma frequency dependence on theta was applied. The number above is computed for Θ=0.

Chapter 6

Conclusion and Future Development

In this chapter, I present two parallel paths of experiments that can be followed by future researchers. A tunable large-scale experiment solution is also presented. Finally, a conclusion on how this experiment could serve the purpose of measuring axion's mass is explained.

6.1 Conclusion

The tunable plasmonic haloscope concept was proposed as a method to reach much higher frequencies but without the sacrifice of conversion volume. It relies on the coupling of the dark matter axion field to a plasmonic oscillation in a metamaterial when the plasma frequency (the effective photon mass) is equal to the axion mass. This thesis accomplished a first limited validation of this concept by showing that a simple wire-array metamaterial does behave as the original theory papers predicted by Pendry [5] and Belov [6]. We were able to confirm earlier limited work by Gay-Balmaz [7] but extended them to an explicit test of the calculations of Belov for the case where square lattice symmetry is broken and the metamaterial is anisotropic, i.e., $b \neq a$. This suggests a possibly practical method for tuning such an array in small, reproducible frequency steps while maintaining a high degree of uniformity of the array, as will be discussed below.

To state the conclusions of this research more precisely:

1. An array of thin wires in free-space represents exhibits behavior that may be described as a high-pass filter.
2. The full plasmonic behavior of these arrays becomes evident with an increasing number of planes of wires; in agreement with Gay-Balmaz et al., it is well-developed by N = 20 for the experimental conditions of our measurements where the plasma frequency was ~10 GHz. We were not able to extend our measurements to N = 25 or more to see if its behavior was already asymptotic or not. At N = 20, if one defines an effective quality factor at the plasma

frequency Q = ω_p/Γ, then Q ~ 200. Absent more measurements with larger wire arrays, corresponding to a larger number of planes, e.g. 50 or 200; it is not possible to say whether this room temperature Q is limited by loss in the wires themselves or whether the dominant loss mechanism is radiation from the surface of the array.

3. Shifting alternating wire planes relative to one another (i.e., changing the wire lattice from rectangular to parallelogram unit cells) does not change the plasma frequency; in fact, there was hardly any discernable change in the S_{21} spectrum at all. This strongly suggests that the only thing that matters is the average density of wires (so long as they remain well-separated, i.e., a >> r). This is good news, as it suggests that local inhomogeneities in wire and plane spacing may be unimportant, so long as there are no long-range gradients in wire density. If so, this will simplify the design and ease fabrication tolerances of an array to be used in the axion experiment.
4. Similarly, changing the angular tilt of the frames relative to the polarization axis does not appreciably change the plasma frequency. But it does drastically raise the noise floor below cutoff, meaning that the high-pass filter character of the array is eroding with angle.
5. The frequency significantly changes when changing the spacing of the planes b, while holding the wire spacing a fixed, in excellent agreement with the calculations of Belov et al. [6].

6.2 Future Development

It is necessary to continue the development of the experiment to qualify it as a measurement method for axion-like dark matter. Future work thus needs to proceed in two directions. The first is to build a 20 frames miniature sample of the setup that could be integrated into our cryogenic test stand to cool the array to 4.2 K to decrease the resistivity of the wires.

Fig. 44 presents a conceptual design of the plasmonic haloscope for the cryogenic test. I suggest the wires be in the form of deposited gold wires on silicon wafers, stacked vertically between two smaller horn antennas.

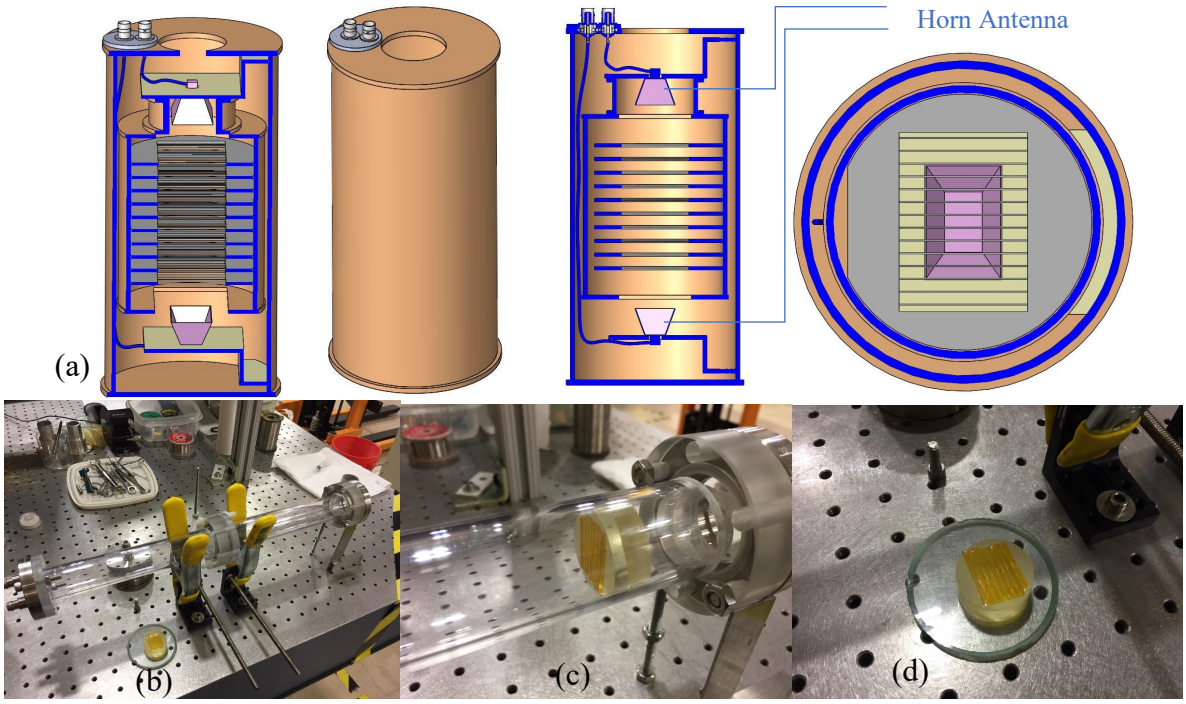

Figure 44: (a) Schematic of a possible cryogenic experiment setup for measuring S_{21} assembled inside our cryogenic test stand, (b) prototype of a cryogenic model with disk insert, (c) disk positioned inside the cylinder, (d) 50 μm wires installed on the surface of the disk.

On the other hand, an actual large-scale detector can be assembled of 50 cm x 50 cm frames with dense wire spacing mounted on thin films of mylar or some other low-loss dielectric. A tuning method can be mechanically achieved by slightly tilting the frames in the x-z-axis in a fine-tuned and controlled motion (stepper motor). The concept of parallel wire planes attached to a pivot mechanism is feasible. By tilting all planes at once at small angles, the plane spacing b will change. Fig. 45 shows a schematic of the large-scale setup. A prototype in its early stages is under development (Fig. 46).

There is a well-developed industry for flexible electronics and making lithographic patterns of copper or aluminum on dielectric sheets is a mature technology. We are beginning to look for suppliers of thin parallel wires patterned on mylar in large rolls.

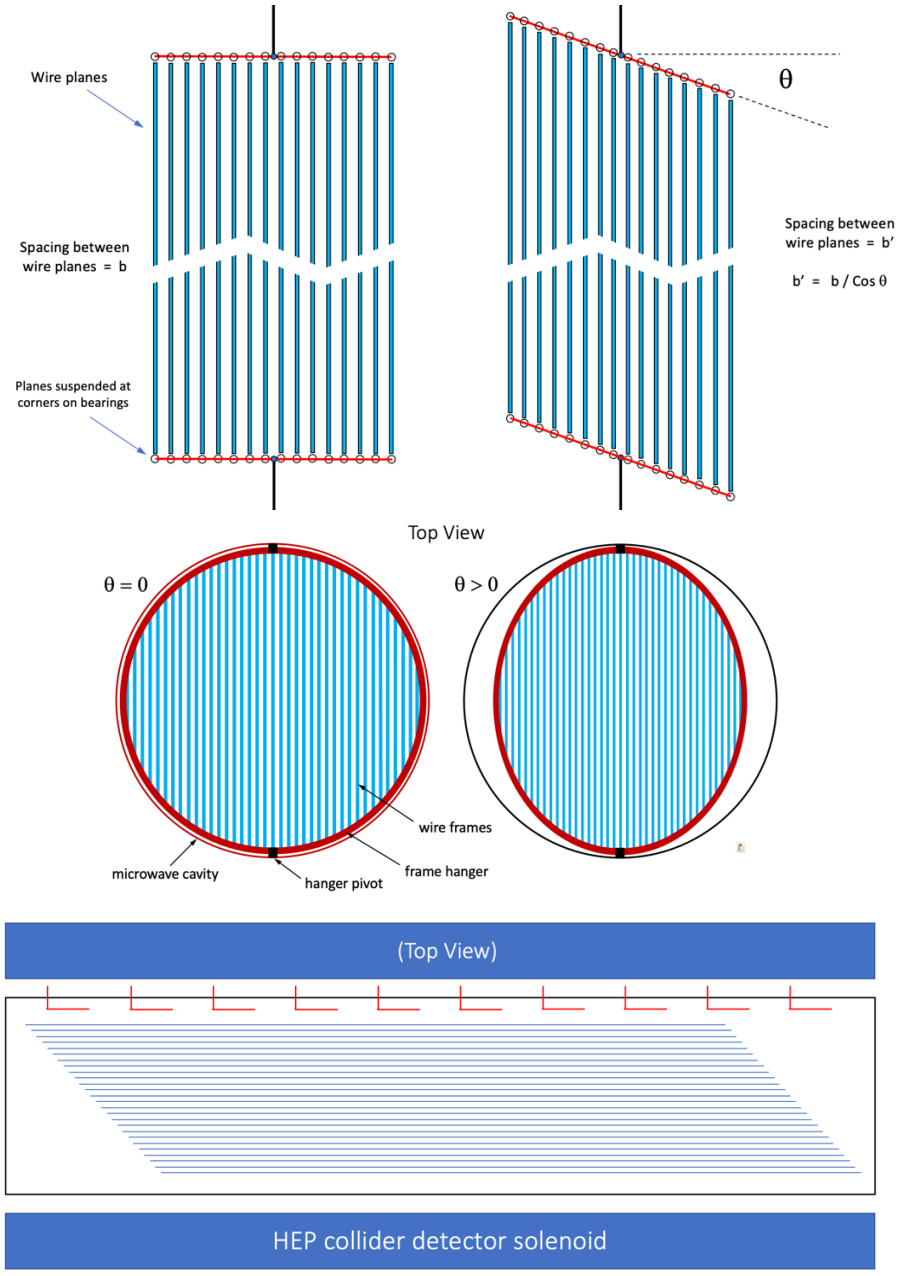

Figure 45: Schematics of large-scale wire array with tuning capability, as suggested by Professor Karl van Bibber.

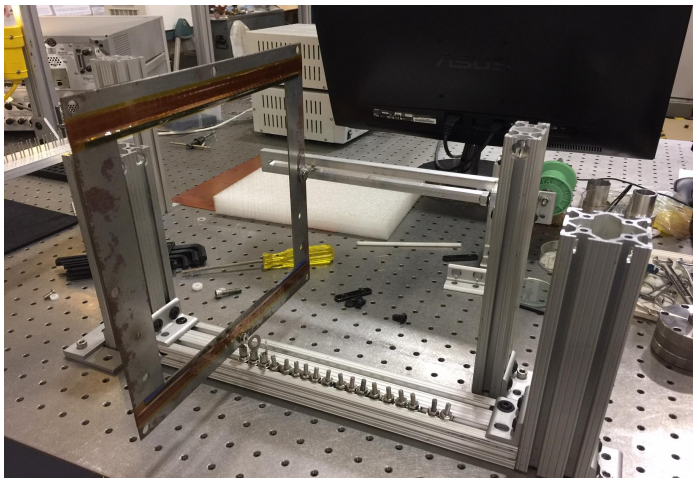

Figure 46: Tunable array prototype under development in our lab.

As an example, a large-scale experiment of 50 cm x 50 cm frames can achieve a resonance frequency of 50 GHz with spacings of a = 1.0 mm, b = 2.0 mm, which corresponds to an axion mass of ~200 μeV. A resonance frequency of 75 GHz at a spacing of a = b = 1 mm can be achieved, which corresponds to 300 μeV. A practical high-density wire spacing[24] of a multi-plane detector inside a magnet bore of 60 cm is feasible.

[24] This is an evaluation of Belov's formula for a = b = 2.5 mm for a gold-coated tungsten wire of 50 μm diameter. If a = b = 1 mm, a frequency of 77.5 GHz can be achieved.

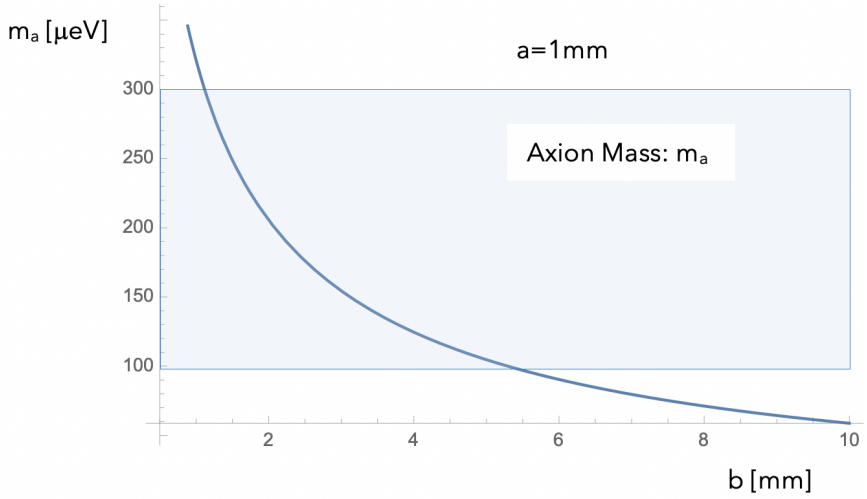

Figure 47: The range of axion masses[25] accessible with an array of a = 1 mm, as a function of b. Such an array would require much thinner frames or wires patterned on a thin-film substrate.

Finally, while this work has helped resolve one of the questions about the tunable plasmonic haloscope, namely the feasibility of a wire array metamaterial as the medium, several other important questions remain to be solved. Most important of them is an antenna design to effectively read out the converted power over the whole volume of the plasmonic medium, given that the Compton wavelength of the axion $l_C = h/m_a c << L$, where L is the dimensions of the array. Another open question is what the most appropriate amplifier technology for the experiment.

[25] Axion mass: m_a [μeV] = 4.136 f [GHz]

Bibliography

1. G. Carosi, G. Rybka and K. Van Bibber (Eds.), Microwave cavities and detectors for axion research, Proceedings of the 2nd International Workshop 2018 (Vol. 211) Springer. (2018).
2. M. Lawson, A. J. Millar, M. Pancaldi, E. Vitagliano, and F. Wilczek, Tunable Axion Plasma Haloscopes, Phys. Rev. Lett. 123, 141802 (2019).
3. P. Drude, Zur Elektronentheorie der Metalle, Annalen der Physik. 306 (3): 566–613 (1900).
4. N. W. Ashcroft, N.D. Mermin, Solid State Physics, Brooks/Cole. (1976).
5. J.P. Pendry, A.J. Holden, D.J. Robbins and W.J. Stewart, Low frequency plasmons in thin wire structure, Journal of Physics: Condensed Matter 10 4785 {4809} (1998).
6. P.A. Belov et al., Strong spatial dispersion in wire media in the very large wavelength limit, Physical Review B, 67(11), 113103 (2003).
7. P. Gay-Balmaz, C. Maccio and O.J.F. Martin, Microwire arrays with Plasmonic response at microwave frequencies, App. Phys. Lett., Vol 81, Number 15 (2002).
8. Y. Sofue and V. Rubin, Rotation curves of spiral galaxies, Annual Review of Astronomy and Astrophysics 39.1 pp. 137–174 (2001) doi: 10.1146/annurev.astro.39.1.137.
9. V.C. Rubin and W.K. Jr. Ford, Rotation of the andromeda nebula from a spectroscopic survey of emission regions, APJ, 159, pp. 379-403. (1970). doi: 10.1086/150317.
10. E. Hubble, Contributions from the Mount Wilson Observatory, Carnegie Institution of Washington, vol. 324. (1931).
11. E. Hubble, A Relation between distance and radial velocity among extra-galactic nebulae, Proc. Nat. Acad. Sci. 15, 168. (1929).
12. G.A. Lemaitre, Homogeneous universe of constant mass and increasing radius accounting for the radial velocity of extra-galactic nebulae, M.N.R.A.S. 41, 483 (1931).
13. J-P. Luminet, Lemaitre's Big Bang, Aix-Marseille Université, CNRS, Laboratoire d'Astrophysique de Marseille (LAM) UMR 7326 and Centre de Physique Théorique de Marseille (CPT) UMR 7332 and Observatoire de Paris (LUTH) UMR 8102, France. arXiv.1503.08304 (2015).

14. M. Boylan-Kolchin and D.R. Weisz, Uncertain Times: The Redshift-Time Relation from Cosmology and Stars, arXiv: 2103.15825. (2021).
15. F. Zwicky, Redshift of Extragalactic Nebulae, Helvetica Physica Acta, Vol. 6, pp 110-127 (1933).
16. L. Baudis and S. Profumo, Dark Matter, Particle Data Group, LBL (2019). https://pdg.lbl.gov/2019/reviews/rpp2019-rev-dark-matter.pdf
17. M. Fukugita, Dark Matter in Galaxies, (ed.) S.D. Ryder, D.J. Pisano, M.A. Walker and K.C. Freeman. San Francisco: Astronomical Society of the Pacific, IAU Symp., 220, 227 (2004).
18. D. Merritt, The Distribution of Dark Matter in the Coma Cluster, Astrophysical Journal v.313, p.121 (1987).
19. J. Audouze (auth.) and P. Crane (eds.), The Light Element Abundances, ESO Astrophysics Symposia (European Southern Observatory). Springer, Berlin, Heidelberg (1995).
20. R. D. Peccei and H.R. Quinn, CP Conservation in the Presence of Pseudo-particles, Phys. Rev. Lett. 38, 1440 (1977).
21. S. Weinberg, A New Light Boson, Phys. Rev. Lett. 40, 223 (1978).
22. F. Wilczek, Problem of Strong P and T Invariance in the Presence of Instantons, Phys. Rev. Lett. 40, 279. (1978).
23. M. Kuster, G. Raffelt and B. Beltr´an (Eds.), Axions, Theory, Cosmology, and Experimental Searches, ISBN: 978-3-540-73517-5 (2008).
24. P.W. Graham, I.G. Irastorza, S.K. Lamoreaux, A. Lindner and K.A. van Bibber, Experimental Searches for the Axion and Axion-like Particles, arXiv: 1602.00039.20 (2016).
25. P. Sikivie, Experimental tests of the invisible axion, Phys. Rev. Lett. 51, 1415 (1983).
26. V.B. Klaer and G.D. Moore, The dark matter axion mass, JCAP 1711 (2017) 049. arXiv:1708.07521 (2017).
27. J.W. Foster, N.L. Rodd and B.R. Safdi, Revealing the dark matter halo with axion direct detection, Phys. Rev. D 97, 123006 (2018).
28. M. Simanovskaia, A. Droster, H. Jackson, I. Urdinaranb and K. van Bibber, A symmetric multi-rod tunable microwave cavity for a microwave cavity dark matter axion search, Rev. of Sc. Inst. 92, 033305 (2021).
29. T. Braine et al. (ADMX Collaboration), Extended Search for the Invisible Axion with the Axion Dark Matter Experiment, Phys. Rev. Lett. 124, 101303 (2020).

30. D. Lee et al. , CAPP-PACE Experiment with a target mass range around 10μeV, Springer Proceedings in Physics, Vol. 245 , 83-87 (2020).
31. B. M. Brubaker, L. Zhong, Y. V. Gurevich, S. B. Cahn, S. K. Lamoreaux, M. Simanovskaia, J. R. Root, S. M. Lewis, S. Al Kenany, K. M. Backes, I. Urdinaran, N. M. Rapidis, T. M. Shokair, K. A. van Bibber, D. A. Palken, M. Malnou, W. F. Kindel, M. A. Anil, K. W. Lehnert, and G. Carosi, First results from a microwave cavity axion search at 24 μeV, Phys. Rev. Lett. 118, 061302 (2017).
32. K. M. Backes, D. A. Palken, S. Al Kenany, B. M. Brubaker, S. B. Cahn, A. Droster, Gene C. Hilton, Sumita Ghosh, H. Jackson, S. K. Lamoreaux, A. F. Leder, K. W. Lehnert, S. M. Lewis, M. Malnou, R. H. Maruyama, N. M. Rapidis, M. Simanovskaia, S. Singh, D. H. Speller, I. Urdinaran, Leila R. Vale, E. C. van Assendelft, K. van Bibber and H. Wang, A quantum enhanced search for dark matter axions, Nature volume 590, pp. 238–242 (2021).
33. G. B. Gelmini, A. J. Millar, V. Takhistov, and E. Vitagliano, Probing dark photons with plasma haloscopes, Phys. Rev. D 102, 043003 (2020)
34. A. Yahalom, Y. Pinhasi, E. Shifman and S. Petnev, Transmission through single and multiple layers in the 3-10 GHz band and the implications for communications of frequency varying material dielectric constants, WSEAS transactions on communications. ISSN: 1109-2742. (2010).
35. J. Preskill, M. B. Wise, and F. Wilczek, Cosmology of the invisible axion, Phys. Lett. 120B, 127 (1983).
36. L. Abbott and P. Sikivie, A cosmological bound on the invisible axion, Phys. Lett. 120B, 133 (1983).
37. M. Dine and W. Fischler, The not-so-harmless axion, Physics Letters B 120.1, pp. 137 –141. ISSN: 0370-2693 (1983).
38. F. Takahashi, W. Yin and A.H. Guth, QCD axion window and low-scale inflation, Phys. Rev. D98, p. 015042 (2018).
39. P. Sikivie, Experimental Tests of the Invisible Axion, Phys. Rev. Lett. 51, 1415 (1983); Erratum, 52, 695 (1984).
40. D.M. Pozar, Microwave Engineering, Fourth Editions, the University of Massachusetts at Amherst, John Wiley and Sons, Inc. (2012).
41. J.D. Jackson, Classical Electrodynamics, Third Edition. Wiley (1999).
42. D. Attwood and A. Sakdinawat, X-rays and Extreme Ultraviolet Radiation: Principles and Applications, Cambridge University Press (2017).

43. D. Pines, Elementary Excitations in Solids, Advanced Book Program. ISBN 0-7382-0115-4 (1999).
44. S.I. Maslovski, S.A. Tretyakov and P. Belov, Wire media with negative effective permittivity: a quasi-static model, Microwave and Optical Technology Letters, 35(1), 47-51 (2002).
45. P. Markoš and C.M. Soukoulis, Absorption losses in periodic arrays of thin metallic wires, Optics Letters, 28(10), 846-848 (2003).
46. E.V. Ponizovskaya, M. Nieto-Vesperinas and N. Garcia, Losses for microwave transmission in metamaterials for producing left-handed materials: The strip wires, Applied Physics Letters, 81(23), 4470-4472 (2002).
47. P. Schneider, Extragalactic Astronomy and Cosmology: An Introduction, Springer, ISBN-10 3-54033174-3 (2006).
48. M. Morrison, C. Hastings and K. Mischo, Hands-On Start to Wolfram Mathematica, (2016).
49. S.H. Simon, The Oxford Solid State Basics, OUP Oxford (2014).
50. B. Brubaker et al., First Results from a Microwave Cavity Axion Search at 24 μeV , Phys. Rev. Lett. 118, 061302 (2017).
51. S. J. Asztalos, R. F. Bradley, L. Duffy, C. Hagmann, D. Kinion, D. M. Moltz, L. J. Rosenberg, P. Sikivie, W. Stoeffl, N. S. Sullivan, D. B. Tanner, K. van Bibber, and D. B. Yu, Improved rf cavity search for halo axions, Phys. Rev. D 69, 011101 (2004).
52. P. Sikivie, Experimental Tests of the Invisible Axion, Phys. Rev. Lett. 51, 1415 (1983).
53. K. Van Bibber, P.M. McIntyre, D.E. Morris and G.G. Raffelt, A practical laboratory detector for solar axions, Phys. Rev. D 39, 2089 204 (1989).
54. D.M. Lazarus et al., A search for solar axions, Phys. Rev. Lett. 69, 2333 (1992).
55. S. Moriyama et al., Direct search for solar axions by using strong magnetic field and X-ray detectors, Phys. Lett. B 434, 147 (1998).
56. G.G. Raffelt, Stars as Laboratories for Fundamental Physics, University of Chicago Press, Chicago (1996).
57. K. Van Bibber, N.R. Dagdeviren, S.E. Koonin, A. Kerman and H.N. Nelson, An experiment to produce and detect light pseudoscalars, Phys. Rev. Lett. 59, 759 (1987).
58. P. Sikivie, D. Tanner and K. Van Bibber, Resonantly Enhanced Axion-Photon Regeneration, Physical Review Letters. 98 (17) (2007).

59. S. Lewis, Photonic bandgap resonators for HAYSTAC, For the HAYSTAC Collaboration. APS April Meeting. Y09.002 (2019).
60. M. Ahlers and F. Halzen, Opening a new window onto the universe with IceCube, Progress in Particle and Nuclear Physics, Volume 102, p. 73-88 (2018).
61. A.C. Melissinos et al., Experience with the Rochester-Brookhaven-Fermilab axion detector, Workshop on Cosmic Axions, p. 39 - 41 (1990).
62. S. De Panfilis et al., Limits on the Abundance and Coupling of Cosmic Axions at 4.5 μeV< ma <5.0 μeV , Phys. Rev. Lett. 59, 839 (1987).
63. C. Hagmann, P. Sikivie, N.S. Sullivan and D.B. Tanner, Results from a search for cosmic axions, Phys. Rev. D 42, 1297(R) (1990).
64. E. Clinton, A precision measurement of the neutral pion lifetime via the Primakoff effect, United States: N. p., doi:10.2172/955702 (2007).
65. Jaco de Swart. Deciphering dark matter: the remarkable life of Fritz Zwicky. Nature 573, 32-33 (2019).
66. K. van Bibber, Scaling up the search for dark matter, APS Physics (2009).
67. G. Charpak, Multiwire and drift proportional chambers, Physics Today 31, 10, 23 (1978). doi: 10.1063/1.2994772
68. E. Aprile et al., The XENON1T Dark Matter Experiment, (2017). arXiv:1708.07051v1

Appendix A: Data Sheets
A.1 Convoluted Foam Absorber

RoHS Compliant

MAST TECHNOLOGIES

Convoluted Foam Absorber

MF32-0002-00

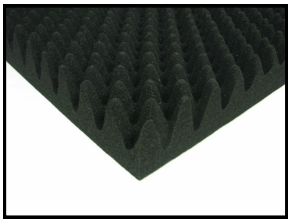

MAST Technologies' Convoluted Foam Absorber product series is a lightweight conductive carbon loaded sheet stock providing broadband reflection loss at microwave frequencies. Due to the shape of the cones on Convoluted Foam Absorbers, they exhibit high reflection loss and are intended to be applied to metal surfaces inside test boxes, housings, radomes, network enclosures, or antennae. Convoluted Foam Absorbers attenuate energy at normal and high angles of incidence at frequencies from 1 GHz to 18 GHz.

APPLICATIONS

RF Test Boxes/Fixtures

Antenna Pattern Performance

Sidelobe/backlobe reduction

Resonant Cavity Attenuation

EMI Reduction

Rx/Tx Antenna Isolation

Radar Cross Section Reduction

FEATURES & BENEFITS

Lightweight foam

Cost effective broadband material

Easily applied with PSA

Most broadband absorber material

RoHS Compliant

Halogen Free

TYPICAL PROPERTIES

Thickness: 3.0" (76.9mm)

Adhesive Thickness: 0.005" (0.12mm)

Color: Black

Operating Temperature: -60°F to 250°F

Flammability Rating: UL94-HF1 Available

PART NUMBERING: MF32-0002-XX

00: No PSA backing

01: PSA backing

>10: Die Cut

ELECTRICAL PERFORMANCE

This performance plot illustrates the Reflectivity performance of this material. Reflectivity is measured in an NRL Arch, for more information on the NRL Arch test set-up, please refer to Tech Bulletin 101. Additional electrical test data may be available upon request.

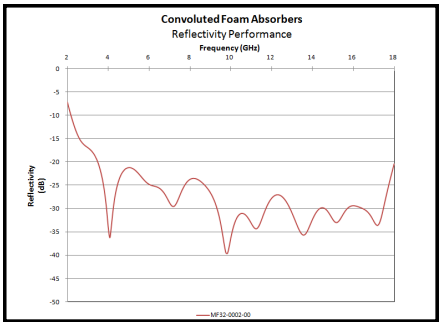

METHOD OF APPLICATION

The primary method of application for Convoluted Foam Absorbers is utilizing a Pressure Sensitive Adhesive (PSA) backing. MAST proudly uses 3M transfer tapes on it's Convoluted Foam Absorbers. Contact MAST technical representatives for a datasheet on the PSA.

Other liquid and paste adhesive may be recommended. Contact a MAST technical representative for more information.

AVAILABILITY

Standard Sheet Sizes: 24" x 24" (615 x 615mm)

Format: Sheets, Die Cut

MAST Technologies

6370 Nancy Ridge Dr.
Suite 103
San Diego, CA 92121
U.S.A.

tel+ 1.858.452.1700

www.masttechnologies.com

Revision: January 20, 2011

Appendix A.2 Tungsten Wire Data Sheet

LUMA METALL®
Fine wire products

Luma Gold Plated Tungsten Wire

For some applications tungsten wire has to be plated to meet special requirements. This may be for instance to protect the wire from corrosion, to solder it to other metals or to reduce the secondary emission of electrons.

Example of applications

- Antennas
- Printing
- Medical
- Connectors
- Technical research
- Fuses
- Bonding

Properties of bare Tungsten wire	
Purity	99.95% W
Melting point	3410 °C
Density	19.17 g/cm^3
Specific electrical resistance at 20 °C	0.055 Ohm x mm^2/m
Modulus of elasticity at 20 °C	410 kN/mm^2

Wire qualities	**Description**
821/60	Treatment before plating: Etched. Type of strike: Gold
821/65	Treatment before plating: Etched. Type of strike: Gold *This quality is processed to meet demands for medical use.*
821/66	Treatment before plating: Ultra polished. Type of strike: Gold
821/67	Treatment before plating: Ultra polished. Type of strike: Nickel

Examples of wire dimensions with coat thickness as per Luma standard

Wire Dimension (microns)	**Wire Dimension (mils)**	**Au coat thickness (microns)**	**Au coat by weight %**
25	0.984	0.25 +/- 0.07	3.0 - 5.0
50	1.97	0.5 +/- 0.1	3.0 - 5.0
75	2.95	0.5 +/- 0.1	2.2 - 3.2
100	3.94	0.5 +/- 0.1	1.6 - 2.4
150	5.91	0.5 +/- 0.1	1.0 - 1.6

2014.03

Data sheet of LM wires.

Appendix A.3 Pasternack Horn Antenna

PASTERNACK®

WR-90 Standard Gain Horn Antenna Operates From 8.2 GHz to 12.4 GHz With a Nominal 20 dB Gain WR-90 Input

TECHNICAL DATA SHEET **PE9856-20**

WR-90 Standard Gain Horn Antenna Operates From 8.2 GHz to 12.4 GHz With a Nominal 20 dB Gain WR-90 Input

Configuration

Design	WR-90 Standard Gain Horn
Frequency Range, GHz	8.2 to 12.4
Polarization	Linear
Interface 1	WR-90

Electrical Specifications

Nominal Gain, dB	20

Mechanical Specifications

Size

Length, in [mm]	10.06 [255.52]
Width, in [mm]	5 [127]
Height, in [mm]	3.7 [93.98]
Weight, lbs [g]	0.75 [340.19]

Compliance Certifications (visit www.Pasternack.com for current document)

Plotted and Other Data

2 Dimensional OML Drawing	PE9856-20
Notes:	Values at 25 °C, sea level

WR-90 Standard Gain Horn Antenna Operates From 8.2 GHz to 12.4 GHz With a Nominal 20 dB Gain WR-90 Input from Pasternack Enterprises has same day shipment for domestic and International orders. Our RF, microwave and fiber optic products maintain a 99% availability and are part of the broadest selection in the industry.

Click the following link (or enter part number in "SEARCH" on website) to obtain additional part information including price, inventory and certifications: WR-90 Standard Gain Horn Antenna Operates From 8.2 GHz to 12.4 GHz With a Nominal 20 dB Gain WR-90 Input PE9856-20

URL: http://www.pasternack.com/standard-gain-horn-waveguide-size-wr90-pe9856-20-p.aspx

Pasternack Enterprises, Inc. • P.O. Box 16759, Irvine, CA 92623
Phone: (866) 727-8376 or (949) 261-1920 • **Fax:** (949) 261-7451
Sales@Pasternack.com • Techsupport@Pasternack.com

Data sheet of horn antenna (1).

PASTERNACK®
THE ENGINEER'S RF SOURCE

WR-90 Waveguide Standard Gain Horn Antenna Operating From 8.2 GHz to 12.4 GHz With a Nominal 20 dB Gain SMA Female Input

Gain Horns with Waveguide to Coax Adapters Tech- PE9856/SF-20

Configuration

Design	WR-90 Standard Gain Horn
Pattern	Directional
Polarization	Linear
Coaxial Interface	SMA Female

Electrical Specifications

Description	Minimum	Typical	Maximum	Units
Frequency Range	8.2		12.4	GHz
Impedance		50		Ohms
Waveguide Standard Gain Horn				
Gain		20		dB
Horizontal Half Power Beam Width		16.5		Degrees
Vertical Half Power Beam Width		16.1		Degrees
Waveguide to Coaxial Adapter				
Input VSWR			1.25:1	

Mechanical Specifications

Size

Weight	5 lbs [2.27 Kg]

RF Connector

Type	SMA Female

Waveguide Interface

Waveguide Size	WR-90

Environmental Specifications

Compliance Certifications (see product page for current document)

Plotted and Other Data

2 Dimensional OML Drawing	PE9856/SF-20
Notes:	

Click the following link (or enter part number in "SEARCH" on website) to obtain additional part information including price, inventory and certifications: WR-90 Waveguide Standard Gain Horn Antenna Operating From 8.2 GHz to 12.4 GHz With a Nominal 20 dB Gain SMA Female Input PE9856/SF-20

Pasternack Enterprises, Inc. • P.O. Box 16759, Irvine, CA 92623
Phone: (866) 727-8376 or (949) 261-1920 • **Fax:** (949) 261-7451
Sales@Pasternack.com • Techsupport@Pasternack.com

A.3-Continue: Data sheet of horn antenna (2).

Appendix A.4 Pasternack Horn Antenna CAD

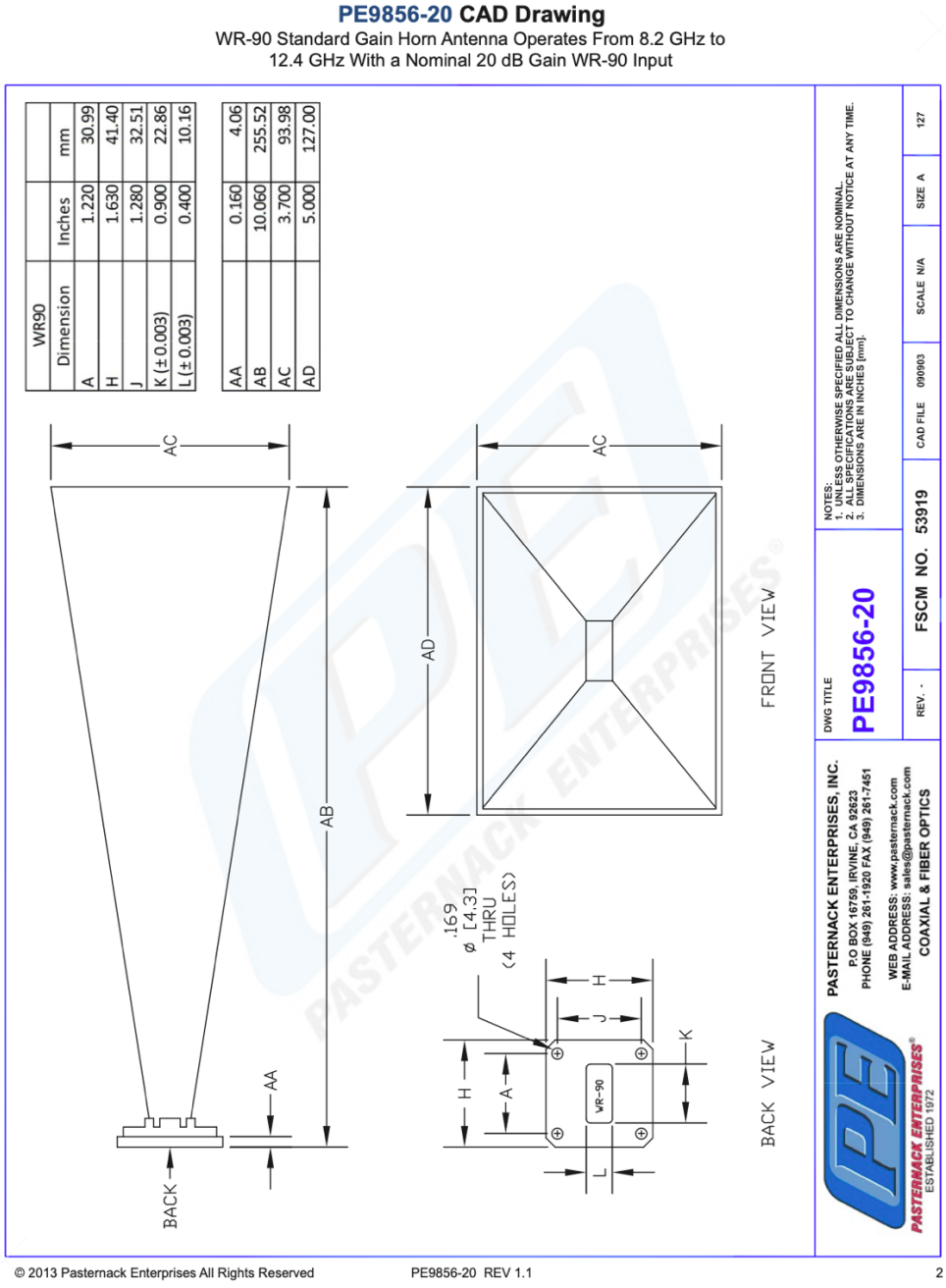

Figure A.1 CAD drawing of horn antenna (1).

Appendix A.5 McMaster Plastic Washer

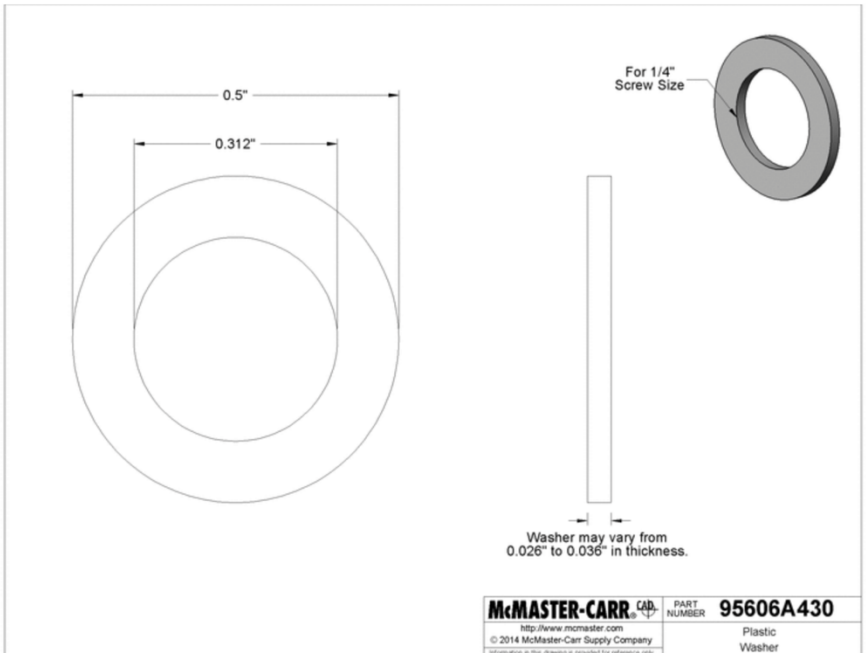

Figure A.5.1 CAD drawing of horn antenna (1).

Sample #	Thickness [mm]
1	.61
2	.61
3	.60
4	.61
5	.61
6	.61
7	.60
8	.61
9	.62
10	.60

Table A.5.2 Washers thickness as measured in the lab.

Appendix B: CAD Drawings

B.1 Frame Assembly CAD.1

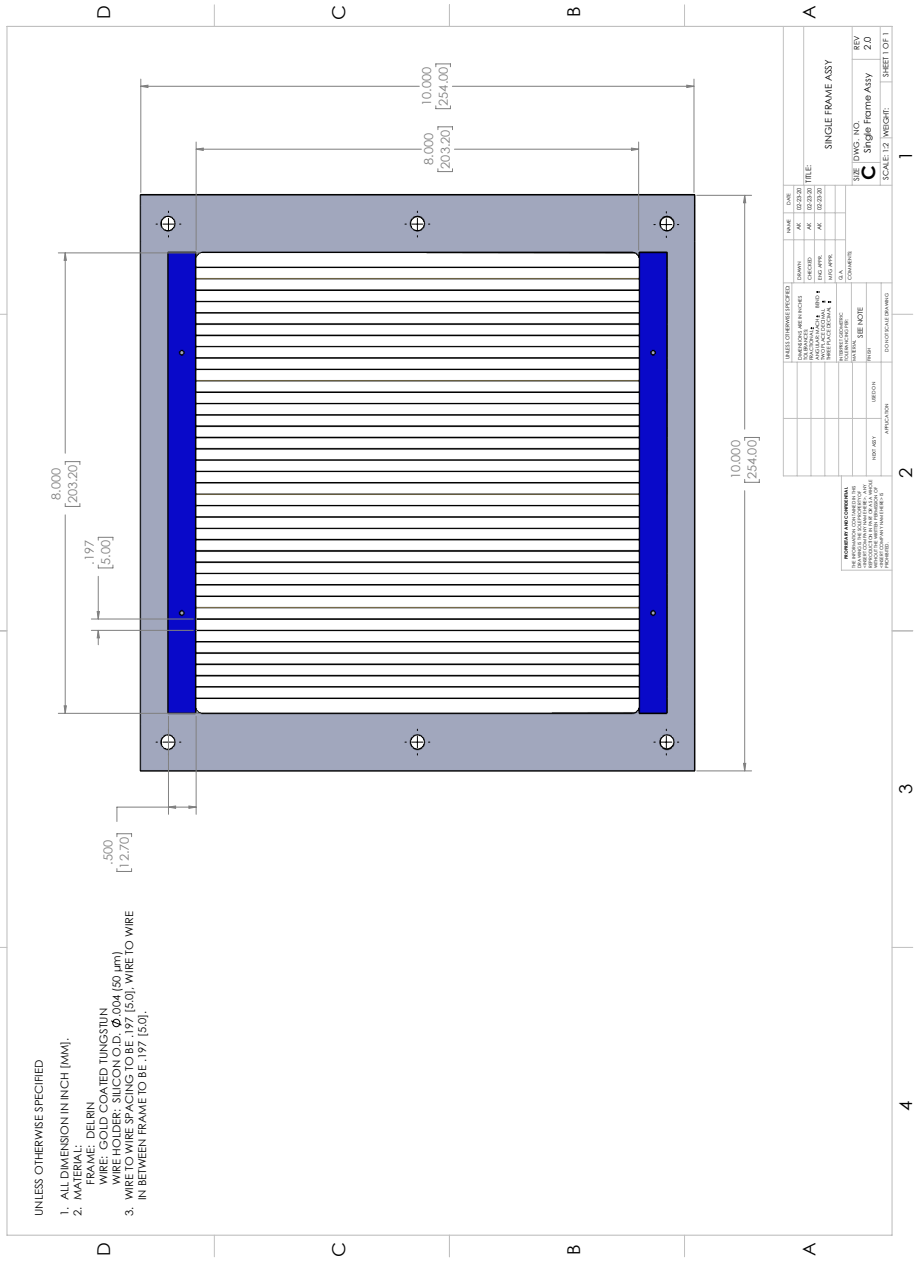

Appendix B.2
Frame Assembly CAD. 2

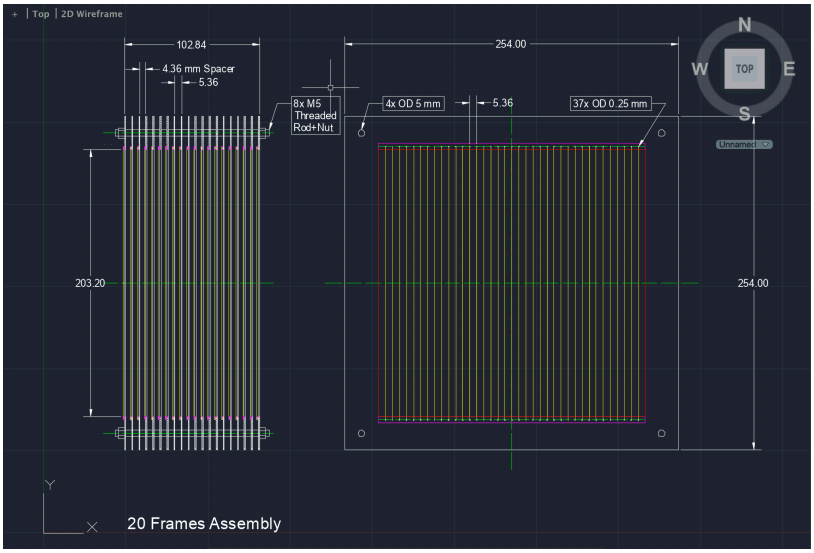

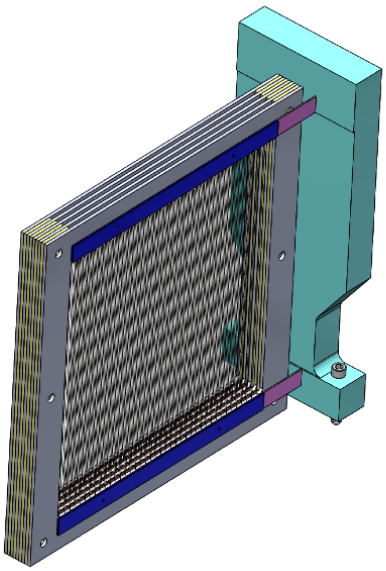

Isometric view of CAD 5-frames assembly

Appendix B.3 Frame Bracket CAD

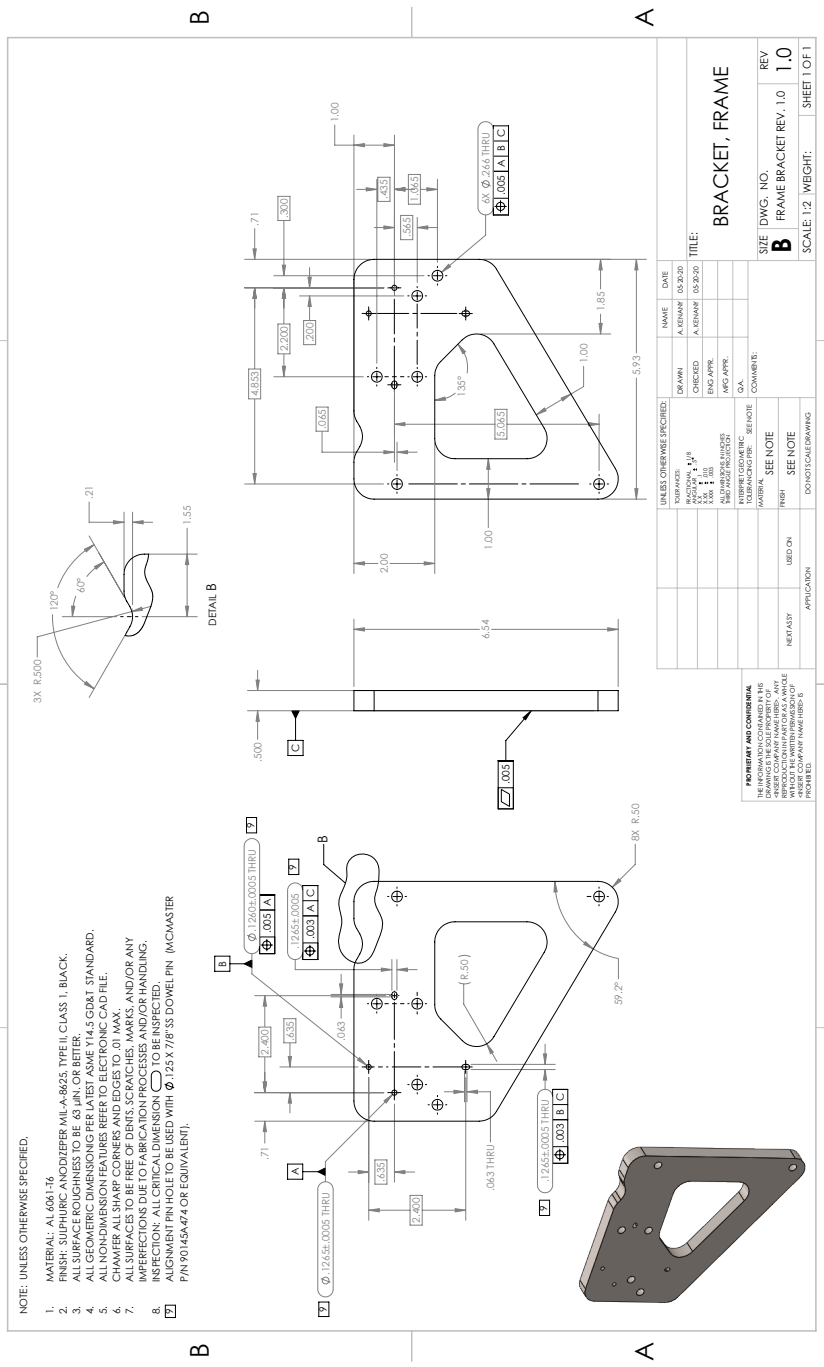

Appendix B.4 Base Bracket CAD

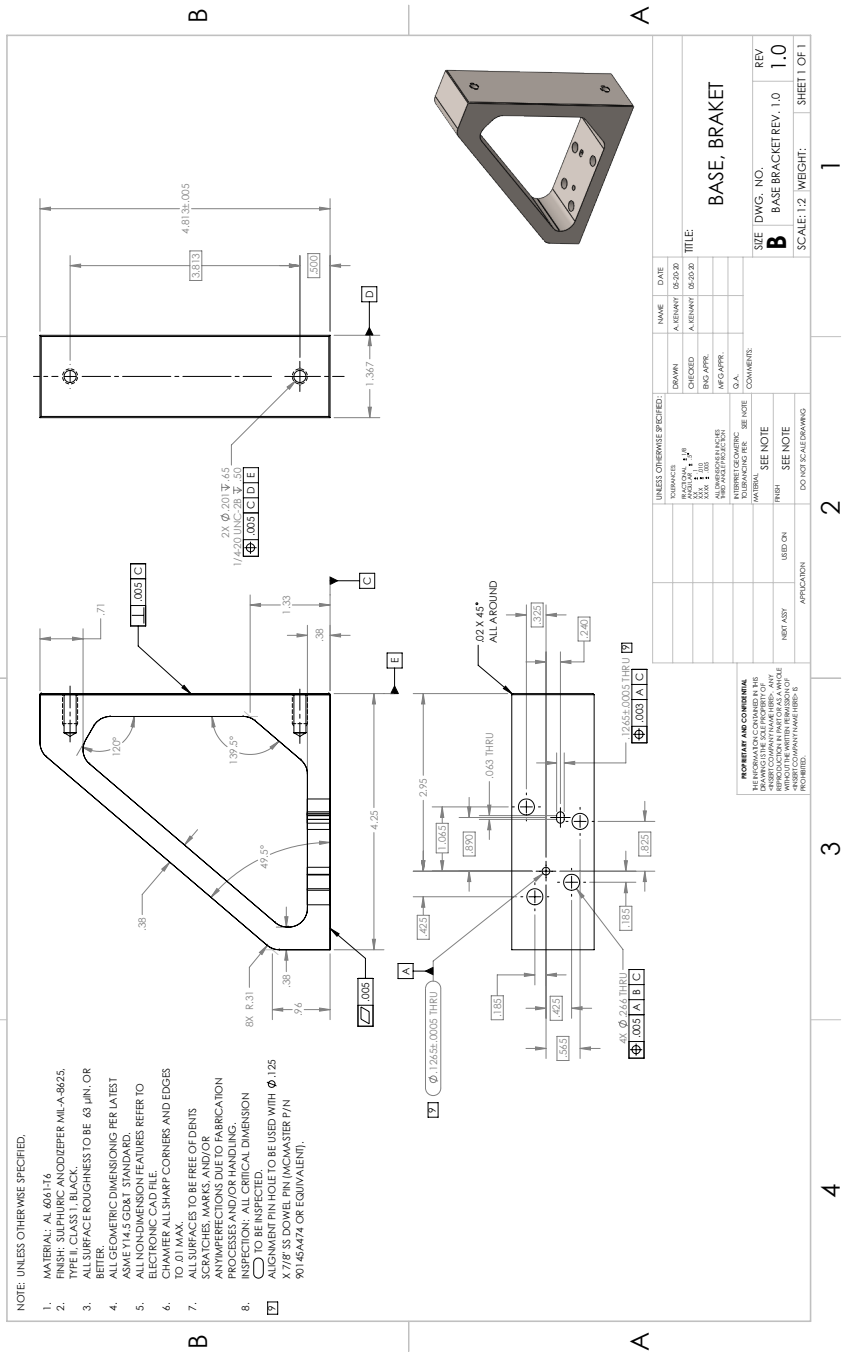

Appendix B.5 Rotational Stage Plate CAD

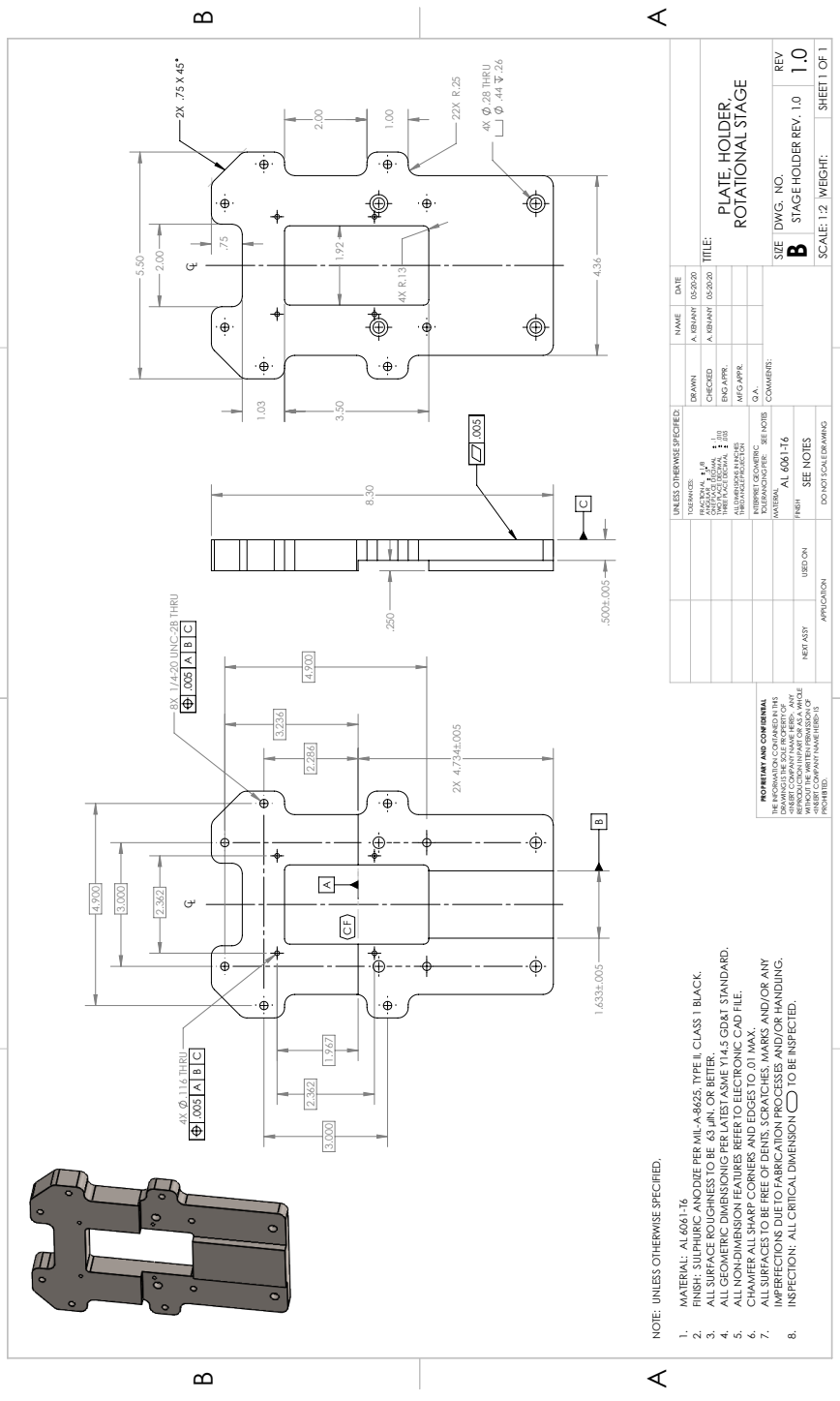

Appendix C: Experiment Photographs

C.1 Experiment Setup Photos

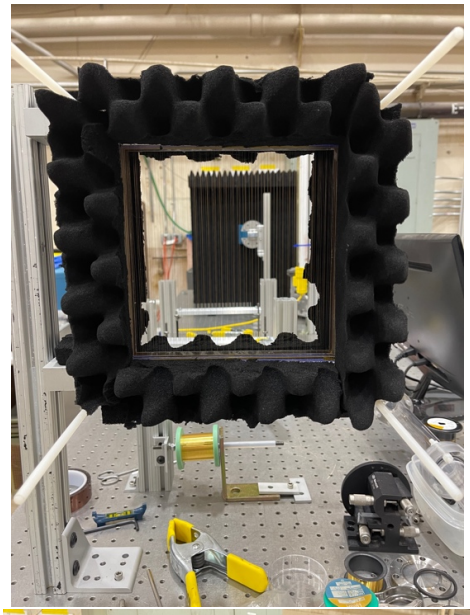

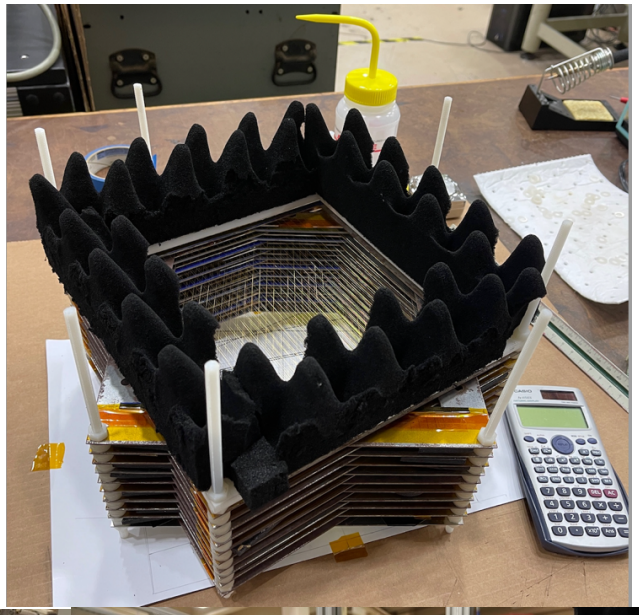

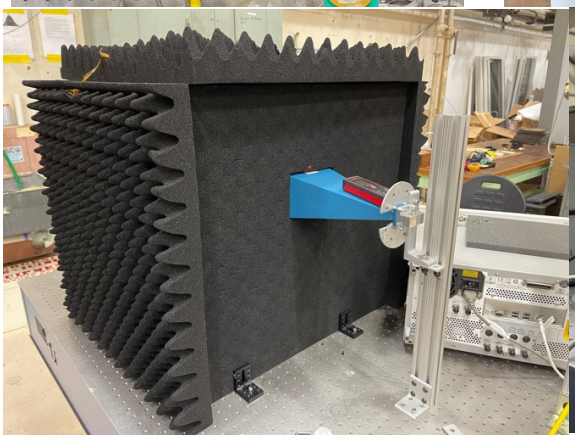

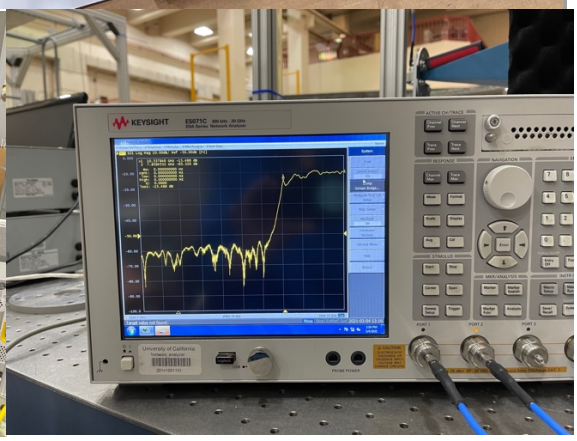

Appendix D: Plots
Results from LSF Plots t=F(b)

2.
Spacers:4 (with b)
{66164.9, {d → 0.0868162, ωp → 12.3118, Γ → 0.115119, b → 0.039

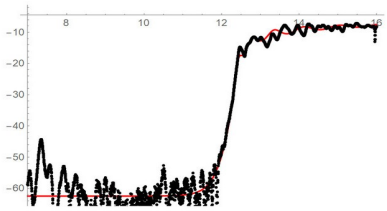

2.
Spacers:4 (with b)
{65373.8, {d → 0.163176, ωp → 12.3359, Γ → 0.17775, b → 0.001637

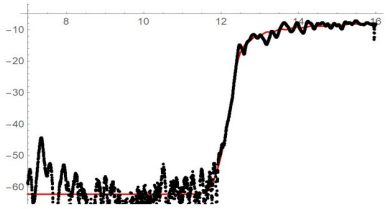

3.
Spacers:6 (with b)
{60725.5, {d → 0.11698, ωp → 10.6197, Γ → 0.0846727, b → 0.0443298

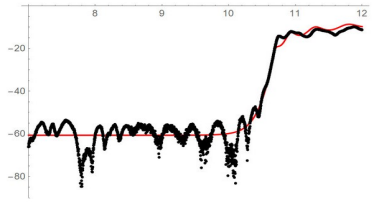

3.
Spacers:6 (with b)
{59391.6, {d → 0.221632, ωp → 10.628, Γ → 0.139151, b → 0.00199

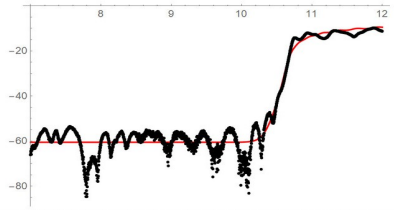

4.
Spacers:7 (with b)
{51043., {d → 0.194152, ωp → 9.88207, Γ → 0.19706, b → 0.0399649}

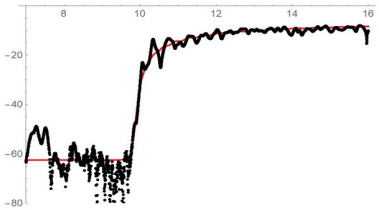

4.
Spacers:7 (with b)
{52306.7, {d → 1.7194, ωp → 9.78784, Γ → 0.0578293, b → 0.00162661}

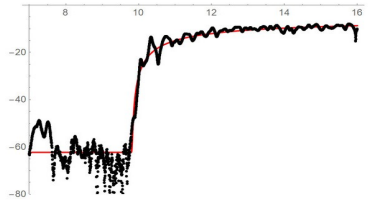

5.
Spacers:7 (without b)
{12598.6, {d → 0.114692, ωp → 9.98824, Γ → 0.278126}}

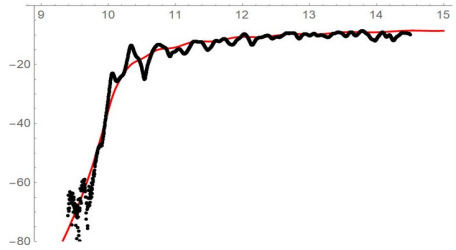

5.
Spacers:7 (without b)
{12844., {d → 0.226157, ωp → 10.0033, Γ → 0.322249}}

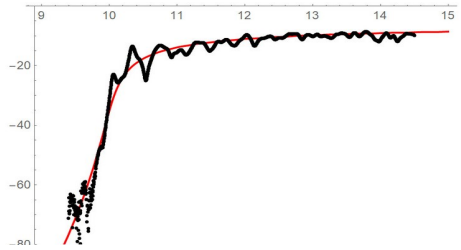

-80

-80